EARTH SURFACE PROCESSES AND LANDFORMS Earth Surf. Process. Landforms (2013)
Copyright © 2013 John Wiley & Sons, Ltd.
Published online in Wiley Online Library
(wileyonlinelibrary.com) DOI: 10.1002/esp.3415

# Probing deep weathering in the Shale Hills Critical Zone Observatory, Pennsylvania (USA): the hypothesis of nested chemical reaction fronts in the subsurface

Susan L. Brantley, 1\* Molly E. Holleran, 1 Lixin Jin 1,2 and Ekaterina Bazilevskaya 1

- <sup>1</sup> Earth and Environmental Systems Institute, Department of Geosciences, Pennsylvania State University, University Park, PA, USA
- <sup>2</sup> Department of Geological Sciences, University of Texas at El Paso, El Paso, TX, USA

Received 13 February 2012; Revised 12 February 2013; Accepted 20 February 2013

\*Correspondence to: Susan L. Brantley, Earth and Environmental Systems Institute, Department of Geosciences, Pennsylvania State University, University Park, PA 16802, USA. E-mail: brantley@eesi.psu.edu



Earth Surface Processes and Landforms

ABSTRACT: Weathering is both an acid-base and a redox reaction in which rocks are titrated by meteoric carbon dioxide (CO<sub>2</sub>) and oxygen (O<sub>2</sub>). In general, the depths of these weathering reactions are unknown. To determine such depths, cuttings of Rose Hill shale were investigated from one borehole from the ridge and four boreholes from the valley at the Susquehanna Shale Hills Observatory (SSHO). Pyrite concentrations are insignificant to depths of 23 m under the ridge and 8–9 m under the valley. Likewise, carbonate concentrations are insignificant to 22 and 2 m, respectively. In addition, a 5–6 m-thick fractured layer directly beneath the land surface shows evidence for loss of illite, chlorite, and feldspar. Under the valley, secondary carbonates may have precipited.

The limited number of boreholes and the tight folding make it impossible to prove that depth variations result from weathering instead of chemical heterogeneity within the parent shale. However, carbonate depletion coincides with the winter water table observed at ~20 m (ridge) and ~2 m depth (valley). It would be fortuitous if carbonate-containing strata are found under ridge and valley only beneath the water table. Furthermore, pyrite and carbonate react quickly and many deep reaction fronts for these minerals are described in the literature. We propose that deep transport of  $O_2$  initiates weathering at SSHO and many other localities because pyrite commonly oxidizes autocatalytically to acidify porewaters and open porosity. According to this hypothesis, the mineral distributions at SSHO are nested reaction fronts that overprint protolith stratigraphy. The fronts are hypothesized to lie subparallel to the land surface because  $O_2$  diffuses to the water table and causes oxidative dissolution of pyrite. Pyrite-derived sulfuric acid (H<sub>2</sub>SO<sub>4</sub>) plus CO<sub>2</sub> also dissolve carbonates above the water table. To understand how reaction fronts record long-term coupling between erosion and weathering will require intensive mapping of the subsurface. Copyright © 2013 John Wiley & Sons, Ltd.

KEYWORDS: weathering; shale; pyrite; carbonates; clays

#### Introduction

Weathering is both an acid-base and a redox titration: basic, electron-rich rocks neutralize and provide electrons to carbon dioxide ( $CO_2$ )- and oxygen ( $O_2$ )-charged meteoric fluids. Over multimillion year timescales globally, the acid-base weathering titration is so significant that it is an important control on the partial pressure of the acid gas,  $CO_2$ , while the redox titration is an important control on the partial pressure of the electron acceptor,  $O_2$ . Three generalized reactions that describe these controls on global p $CO_2$  and p $O_2$  were discussed as early as the 1800s (Ebelmen, 1845; Berner, 2006):

$$CO_2 + (Ca, Mg)SiO_3 \Leftrightarrow (Ca, Mg)CO_3 + SiO_2$$
 (1)

$$CH_2O + O_2 \Leftrightarrow CO_2 + H_2O$$
 (2)

$$15O_2 + 4FeS_2 + 8H_2O \Leftrightarrow 2Fe_2O_3 + 8SO_4^{2-} + 16H^+$$
 (3)

Reaction 1 represents the long-term control on atmospheric  $pCO_2$  as the balance between silicate weathering (left to right) and volcanic and metamorphic degassing (right to left). Reaction 2 describes how fixation of carbon into organic matter releases  $O_2$  to the atmosphere (right to left) or how consumption of  $O_2$  during decomposition of organic matter releases  $CO_2$  (left to right). The final reaction represents an additional control on  $pO_2$  due to weathering or decomposition of pyrite (left to right) or pyrite formation (right to left). Importantly, it is well known that many of these reactions are catalyzed by biota, including the sulfur reactions (Nordstrom, 2000; Calmels *et al.*, 2007).

The long-term effects of Reactions 1–3 as they control  $O_2$  and  $CO_2$  in the global atmosphere over geologic time are recorded in the weathered soil profiles developed on the continents. Weathering reactions consume  $CO_2$  and  $O_2$  as the atmospheric gases diffuse into the subsurface. For example,  $pO_2$  varies today from atmospheric values of 0·2 bar at the surface down to extremely low values ( $\leq 10^{-80}$  bar) for fluids at

depth that are equilibrated with igneous rocks. Likewise, pCO<sub>2</sub> varies from levels as high as  $\sim 10^{-2}$  bar at depths where soil respiration (Reaction 2) is significant down to low values such as  $\sim 10^{-5}$  bar for fluids equilibrated with carbonate-poor igneous rocks at depth. The extents of the proton and electron titrations are recorded as mineralogical or elemental variations with depth which can be referred to as reaction fronts. Where the erosion rate is very low, these reaction fronts can propagate downward over time; in contrast, where erosion rates are balanced by the rates of weathering advance, the reaction fronts can be maintained at a constant depth (Brantley and Lebedeva, 2011).

We do not understand the full depth record of consumption of O<sub>2</sub> and CO<sub>2</sub> under exposed land surface due to the heterogeneities of the land surface and underlying lithology as well as the expense of drilling and the ambiguities inherent to geophysical observations of the subsurface. It is likely that the geometry of these reaction fronts mimics surface topography (Chigira, 1990; Drake et al., 2009). In this paper we explore the idea of nested acid-base and redox reaction fronts by studying changes in mineralogy and elemental chemistry versus depth in one small watershed, the Susquehanna Shale Hills Observatory (SSHO). In the SSHO, a large hydrological, geomorphological, and geochemical data set is available. Jin et al. (2010, Jin et al., 2011a, 2011b) have already documented many of the major mineral transformations occurring in the Rose Hill Shale by analyzing soils and cuttings from one ridgetop borehole. They hypothesized that their data document reaction fronts under the ridgeline for ankerite dissolution between 21 and 24 m depth, feldspar dissolution between 6 and 0 m, and illite + chlorite dissolution between 0.5 and the land surface (Brantley et al., 2011). Here, we report measurements of sulfur (i.e. Reaction 3) versus depth for the ridgetop borehole and compare the chemistry of the ridge borehole to that of four valley boreholes to investigate the geometry of consumption of CO<sub>2</sub> and O<sub>2</sub> in the subsurface in the valley. While we cannot prove that mineralogical variations in the subsurface are due to weathering reactions given the complex structure of the stratigraphy underlying the watershed, we show how the data can be interpreted in the context of nested subsurface weathering fronts.

# **Terminology**

It is difficult to define categories of material across a weathering gradient precisely because the physical and chemical characteristics often vary smoothly with depth. At SSHO, weathering progresses from relatively unfractured and chemically unaltered protolith or parent material ('bedrock') to intact and in-place rock that is somewhat fractured and geochemically altered ('saprock') to unconsolidated materials which are highly altered ('regolith'). This usage for 'saprock' differs from that used by researchers from more arid climates (e.g. Graham *et al.*, 2010): here it refers to the zone of the subsurface rock that has been chemically altered to a significant extent (i.e. depleted in carbonate minerals such as ankerite) but is not disaggregated like a soil.

To employ the terms, operational definitions are used. Bedrock is defined as material that must be drilled with a diamond bit using gasoline or electrical power. Saprock is material that shows evidence of weathering but which must be similarly drilled or sometimes be pried apart and sampled with a pick. Finally, regolith is used here to mean only material that can be augered by hand. On the planar hillslopes in the SSHO previously investigated (Jin *et al.*, 2010; Ma *et al.*, 2011a, Ma *et al.*, 2011b), the regolith shows evidence of downslope movement at all positions (except, perhaps, the deepest depths near the valley floor). In this case, therefore, regolith is mostly identical to 'mobile soil'.

#### **Methods**

#### Site description

Located within the Valley and Ridge province in central Pennsylvania, the SSHO experiences a temperate climate and mean annual temperature of 10 °C (Lin, 2006; Anderson et al., 2008; Jin et al., 2010). The area is typically snow-covered from December to mid March. The elevation of the catchment ranges from 310 m at the highest point to 256 m at the outlet (Lin, 2006). The catchment is V-shaped with relatively planar hillslopes that are intersected by several well-developed swales (Figure 1). The catchment is oriented east-west, and is defined

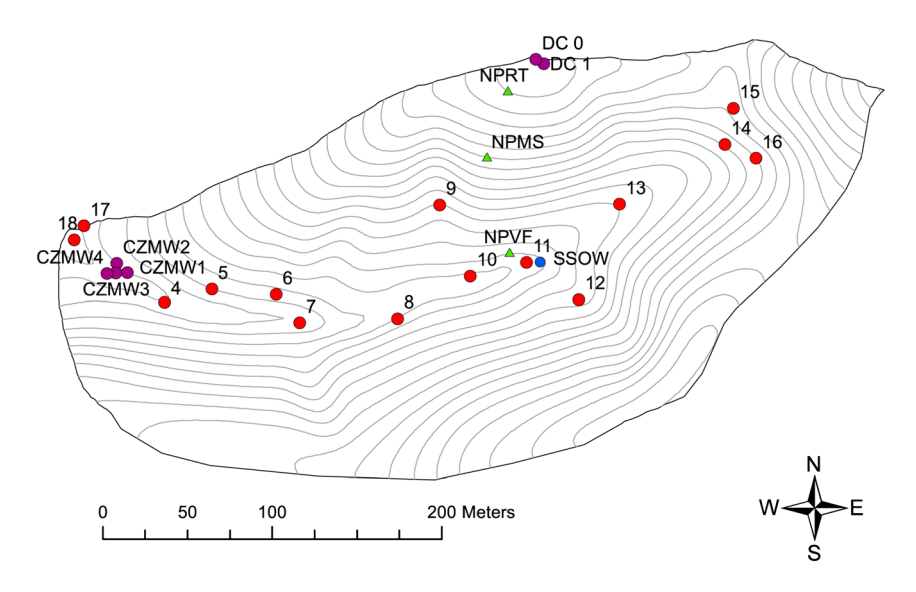


**Figure 1.** Map of Susquehanna Shale Hills Observatory (SSHO). SSHO is an 8-ha forested watershed located in Huntingdon County, PA. Cuttings were sampled from boreholes CZMW1, CZMW2, CZMW3, and CZMW4, labeled as purple circles (see Kuntz *et al.*, 2011): samples were labeled DC2, DC3, DC4, and DC5 respectively. DC1 samples derive from the borehole located at the northern ridge top within 5 m of DC0 (both as purple symbols). Red symbols indicate shallower wells for which no cuttings are available but for which water table levels were measured (Table X). Thin gray lines indicate elevation contours (from Lin, 2006). North planar transect location is shown as three triangles, and the upper weir location is labeled as SSOW (for samples summarized in the Appendix, Table A). This figure is available in colour online at wileyonlinelibrary.com/journal/espl

by the north-facing and south-facing slopes and a small seasonally flowing first-order stream (Lin, 2006).

The underlying protolith consists of relatively tight folds in Silurian-aged shales of the Rose Hill Formation of the Clinton group (Fold, 1960; Lynch, 1976). This group varies in thickness in the area from 200 to 300 m and has been observed locally to sometimes exhibit folds as tight as meters to decimeters (T. White, personal communication, 2012). Although bedrock is almost completely buried throughout the watershed, at one location roughly in the middle of the catchment, limited observations of strike and dip document N54°E and 76°NW respectively (Jin *et al.*, 2011b). However, consistent with the tight folding, a televiewer has been used to measure a dip of ~28° in bedrock in the boreholes drilled at the valley floor near the outlet (Kuntz *et al.*, 2011).

The Rose Hill formation in the area grades from shale to siltstone. In some places the unit is carbonate-rich and occasionally has sandstone layers. In addition, some parts of the Clinton group have enough hematite that it was mined for iron in the 1800s. At SSHO, weathered float from a younger unit, the Keefer sandstone, has been observed toward the valley floor outlet of the catchment.

## Drill core

A borehole at the northern ridge of the catchment, DC0, was drilled prior to the establishment of the Critical Zone Observatory and cased at the top with metal casing. No cuttings are available from that hole but water table measurements are reported here. A second ridgetop borehole was drilled in 2006, approximately 5 m away from DC0, and cased with PVC (DC1). This borehole cannot be used to measure water table due to its construction. Geochemical and mineralogical analyses of the bulk cuttings from DC1 were reported previously (Jin *et al.*, 2010; Ma *et al.*, 2011a).

At the valley floor, four boreholes were drilled with a direct rotary air drill to depths of 16 m in August 2008 (Kuntz *et al.*, 2011). Samples from these four holes [CZMW1, CZMW2, CZMW3, CZMW4 (Figure 1)] are labeled as DC2, DC3, DC4, DC5 samples respectively. The boreholes were drilled within 3 m of one another – three on the northern and one on the southern side of the stream. This study reports chemical and mineralogical results focused on DC3 samples, with additional data from DC2, DC4, and DC5, and new data for the DC1 ridgetop borehole. Samples from DC5 were only retained from depths below 9 m.

Rock chips, cuttings, and rock powder were sampled during drilling in the upper parts of valley boreholes at  $\sim 0.2$  m intervals and at greater depths, approximately every meter. The height of the exposed casing was used to correct depth measurements to depth below land surface (BLS).

#### Sample preparation and elemental analysis

Cuttings were bagged, labeled, and air-dried. For each sample, the entire bulk sample, consisting of both rock fragments and granular powder, was ground to pass a 100-mesh sieve (150  $\mu$ m). Samples were prepared for lithium metaborate fusion according to published methods to determine bulk chemical analysis by inductively coupled plasma atomic emission spectroscopy (ICP-AES) for major elements at the Materials Characterization Laboratory (MCL) at the Pennsylvania State University (Feldman, 1983). These analyses for major elements are estimated to have a precision of  $\pm 3\%$ . This treatment for DC2, DC3, DC4 and DC5 samples was identical to that used

previously for DC1 (Jin *et al.*, 2010, 2011b). However, here, zirconium (Zr) concentrations are reported for analyses by ICP-AES with  $\pm 10\%$  precision while those reported for DC1 were measured by ICP-mass spectrometry (ICP-MS) with  $\pm 5\%$  precision. Accuracy of ICP-AES measurements has been verified for samples from SSHO by a comparison of ICP-AES values to Zr concentrations measured by ICP-MS (Appendix, Table AI). Zr is known to occur in zircons in the catchment (Jin *et al.*, 2010).

#### X-ray diffraction (XRD) analysis

Samples were characterized using X-ray diffraction (XRD). Mineral phases were identified with JADE software and abundances were quantified using US Geological Survey (USGS) software (RockJock), following published protocol (Eberl, 2009). An internal standard of corundum was used in each sample to allow quantification of XRD peaks. Samples were run on a Scintag 2 PAD-V power X-ray diffractometer, scanned from 5° to 65° 2θ, using Cu K-alpha radiation, again following protocol (Eberl, 2009).

## Sulfur, iron and carbon measurements

Total sulfur concentrations were measured using a LECO Sulfur Coulometer. Roughly 400 mg of sample were weighed into ceramic crucibles combined with tin and iron beads as combustion additives following techniques used for coal and plant matter (Jones and Isaac, 1972). The crucible was combusted in an induction furnace and the released sulfur dioxide (SO<sub>2</sub>) gas was titrated with a potassium iodate (KIO<sub>3</sub>) solution. To ascertain accuracy and precision, one calibration standard of known sulfur content (0.889% carbon; 0.0288% sulfur) manufactured by LECO was analyzed repeatedly and one low-sulfur quartz diorite sample (LGW1 85) was analyzed in our laboratory and by LECO, Inc. at their laboratory.

Ferrous iron concentrations were also titrated (Goldich, 1984). References for ferrous iron from the USGS were also analyzed: SCO-1 (Cody shale) was run interspersed with the DC sample analyses reported here and references MAG (marine sediment), GXR2 (soil), and GXR5 (soil) were also analyzed identically over months to assess precision and accuracy.

Total carbon content was measured on DC3 samples by combustion at the Agricultural Analytical Services Laboratory at the Pennsylvania State University, following published protocol (Nelson and Sommers, 1996). We report the wt% total carbon where total carbon = organic + inorganic carbon.

Concentrations and isotopic compositions of total carbon (organic + inorganic) in selected samples were also measured for cores DC1 and DC3 using a Coztech Elemental Analyzer and a Thermo Gas Bench, respectively, in the Laboratory for Isotopes and Metals in the Environment at Pennsylvania State. A low-carbon soil reference material was analyzed as a check standard.

#### Porosity analysis

To analyze porosity in borehole samples, two shale chips from the DC1 core were studied: DC1-36 and DC1-9. The ~1 mm  $\times$  3 mm  $\times$  3 mm pieces were chipped off of larger fragments by breaking perpendicular to bedding. Their porosity was imaged and quantified using synchrotron X-ray-based 3-D  $\mu$ -computed tomography ( $\mu$ -CT) at Beamline 8.3.2 at the Advanced Light Source, Lawrence Berkeley National Laboratory.

The sample was mounted on a specifically designed sample holder and illuminated by X-rays of 25 keV. These X-rays penetrate the sample but are attenuated as a function of density: lower density material (pores) attenuate X-rays to a lesser degree, allowing imaging of the pore structure. The X-ray detector was used with 1.7 μm/pixel 0.9 and μm/pixel resolution for DC1-36 and DC1-9 samples respectively. Filtered back-projection tomographic reconstruction (Kak and Slaney, 1988) was carried out using Octopus software (Masschaele et al., 2005). Reconstructions of the images were completed to yield views of sections oriented parallel to bedding. Selected images were further treated by anisotropic diffusion filtering, image smoothing, threshold-based segmentation, and skeleton analysis. Skeleton analysis, also referred to as analysis of the medial axis, is used to visualize the network of interconnected one-dimensional paths or branches for transport that can be imaged at scan resolution (Liang et al., 2000). All image analysis was performed using ImageJ software (Abramoff et al., 2004).

#### Measurement of water table depth

The depth to the water table was measured at a subset of wells (Figure 1) with a flat tape water level meter equipped with a submersible probe (Solinst®).

#### Results

#### Borehole observations

Major element concentrations from DC1 samples from the ridge (Figure 1) were reported previously (Jin *et al.*, 2010). As described by Jin *et al.* (2010), the upper 10–30 cm was regolith (in other words, hand augering was possible to that depth). Below that, drilling was required to sample saprock or bedrock. Densities of chips recovered as cuttings were highly variable in the upper 6 m. Samples were generally olive or olive gray in color above 23 m and gray below that. One olive brown sample from 4·5 m had higher values of loss on ignition (LOI) and iron.

In contrast, at CZMW1–CZMW4 in the valley (e.g. sample sets labeled DC2–DC5), hand augering was possible to about the depth of the water table, ~2 m. Below that, drilling was needed. Drilling at the valley floor was notably slower below ~6 m than above that depth (Kuntz *et al.*, 2011). Valley-floor samples from depths shallower than 7 to 8 m were brownish in color while deeper samples were dark gray.

# Bulk chemistry: choice of immobile element and parent composition

Compositions of the valley floor boreholes are reported in Tables I–IV and a plot from one borehole (samples DC3) is shown in Figure 2. Inspection of Figure 2 and Tables I–IV documents relatively small variations in most major element concentrations compared to the variations in calcium. Calcium concentrations are insignificant in the upper 2 m.

To interpret the chemical data, we first sought an element that is not soluble – i.e. an immobile element that could be used as a reference. We assumed Zr, present in the insoluble mineral zircon at Shale Hills, is immobile and is present throughout the section in a relatively constant concentration. Jin *et al.* (2010) previously documented that Zr is more immobile than all other elements including titanium at Shale Hills.

More difficult to constrain than an immobile element is the composition of the parent material (including its Zr concentration). Jin *et al.* (2010) successfully modeled weathering in SSHO by assuming that the parent shale composition for the entire 8-ha catchment was equivalent to the average of deep borehole cuttings from ridgetop location DC1 (Figure 1), excluding the deepest carbonate-bearing samples from beneath 22 m and the high-iron composition at 4-5 m depth. Importantly, this parent composition defined by borehole DC1 was shown to have a composition within  $\pm 1\sigma$  of all the bottom-most samples of regolith collected by hand-augering cores throughout SSHO. We therefore use the same parent composition here for interpretations of DC1.

However, for the new valley boreholes investigated here, we averaged the bottom seven samples each for DC2, DC3, and DC4 cuttings together with all five deep samples from DC5. Notably, DC2, DC3, DC4 and DC5 samples derived from wells that were spaced within 5 m and their deep layers are arguably a better estimate of parent for this location in the watershed (Figure 1). As discussed later for Figures 8 and 9, we did see evidence that the bottommost sample from two boreholes may have intersected the Keefer formation (a sandstone which is occasionally observed as weathered float at the outlet of the catchment). Nonetheless to be conservative, this sample was included in the calculation of parent. Presumably, the calculated extents of depletion would be larger if we excluded those samples from calculated parent.

Using this parent material (see Tables I–IV), we calculated the mass transfer coefficient  $\tau_{i,j}$  to assess loss or gain of elements relative to the assumed parent composition (Brimhall and Dietrich, 1987; Anderson *et al.*, 2002):

$$\tau_{i,j} = \frac{C_{j,w}C_{i,p}}{C_{i,p}C_{i,w}} - 1 \tag{4}$$

Here, C is the concentration of mobile element j or immobile element i in the parent (subscript p) or weathered material (w). Positive  $\tau_{i,j}$  values indicate enrichment of the element of interest j in weathered material with respect to i in the parent. Negative  $\tau_{i,j}$  values indicate depletion of j with respect to i in the parent. Values of zero indicate no change of the element with respect to Z in the parent, and values of Z indicate 100% depletion.

Table V summarizes  $\tau_{Zr,j}$  values for DC3 samples. Significant depletion of aluminum (Al), calcium (Ca), iron (Fe), potassium (K), magnesium (Mg), sodium (Na), phosphorus (P) and silicon (Si) are observed at the land surface. Variations with depth are discussed in subsequent sections.

# Sulfur, iron, and pyrite

For DC1 and DC3 samples, measured values of total ([Fe<sub>Total</sub>]) and ferrous iron concentrations ([Fe<sup>2+</sup>]) are reported in Table VI and sulfur concentrations in Table VII. [Fe<sup>2+</sup>] was subtracted from [Fe<sub>Total</sub>] (analyzed by lithium metaborate fusion and ICP-AES), to calculate ferric iron concentrations, [Fe<sup>3+</sup>] (Table VI):

$$\left[ Fe^{2+} \right] + \left[ Fe^{3+} \right] = \left[ Fe_{Total} \right] \tag{5}$$

Based on all analyses for all USGS references as summarized in Table VI, the reproducibility in  $[Fe^{2+}]$  varies with iron and organic matter content. For example, for USGS reference SCO-1 (Cody shale) reproducibility was  $\pm 3\%$ ; therefore, most core samples (which contained minimal organic material)

Elemental concentrations for DC2 samples from borehole CZMW1 Table I.

Sample ID	Depth (m BLS)	Al (wt%)	Ca (wt%)	Fe (wt%)	K (wt%)	Mg (wt%)	Mn (wt%)	Na (wt%)	P (wt%)	Si (wt%)	Ti (wt%)	Zr (ppm)	LOI <sup>b</sup> (wt%)
DC 26-7	-1.98	11.1	0.25	5.73	3.94	98.0	0.05	0.25	0.05	26.9	0.62	205	5
DC 27-8	-2.29	11.0	0.24	2.66	3.74	0.89	60.0	0.33	0.03	27.3	0.61	230	4.6
DC2 8-8·5	-2.52	11.5	0.26	5.71	4.01	0.95	0.07	0.31	0.05	26.7	0.62	190	4.4
DC2 9-9.5	-2.82	10.4	0.59	5.23	3.6	0.89	0.07	0.3	0.04	27.5	0.61	225	5.7
DC2 11-13	-3.66	10.2	2.81	4.7	3.51	98.0	60.0	0.34	0.04	25.8	0.59	220	7.5
DC2 13-14	-4.12	9.6	4.47	5.62	3.3	0.93	0.12	0.29	0.04	24.5	0.55	200	8
DC2 14-15	-4.42	10.7	2.07	5.82	3.77	66.0	0.07	0.28	0.03	25.2	0.58	180	8.9
DC2 17-18	-5.34	10.9	1.19	5.6	3.86	1.04	0.1	0.31	0.04	26	0.56	195	9
DC2 22-23	98-9-	8.2	6.73	5.15	2.85	1.2	0.17	0.27	0.05	23.4	0.48	245	10.5
DC2 24-25	-7.47	10.5	1.76	6.2	3.64	1.21	0.11	0.29	0.03	26.4	0.56	225	4.4
DC2 26-27	-8.08	10.7	1.71	6.02	3.71	1.18	0.08	0.3	0.03	25.1	0.58	200	7.1
DC2 31-32	9.6-	11.3	0.74	5.78	3.98	1.15	0.05	0.32	0.04	26.6	0.62	170	3.9
DC2 36-37	-11.13	11.4	0.91	5.5	4.15	1.15	90.0	0.33	0.04	26.4	0.64	170	4.2
DC2 41-42	-12.65	11	0.87	2.66	3.84	1.09	0.05	0.3	0.03	27.3	0.65	190	3.5
DC2 46-47	-14.18	11.2	0.45	5.68	4.03	1.13	0.03	0.32	0.04	27.1	0.65	180	3.5
DC2 51-52	-15.7	10	1.11	5.56	3.41	1.07	90.0	0.27	0.05	28.3	0.55	230	3.6
Parent <sup>a</sup>		10.9	1.09	5.57	3.9	1.14	90.0	0.3	0.04	26.4	0.59	183	
Standard deviation		0.4	0.42	0.24	0.2	0.07	0.02	0.02	0.02	0.7	0.03	35	
Parent DC1 <sup>c</sup>		10.7	0.17	5.49	3.83	1.06	0.07	0.34	0.05	26.7	0.61	171	
Standard deviation		9.0	0.01	0.31	0.22	60.0	0.02	0.03	0	0.4	0.04	16	

<sup>a</sup>Parent for DC2 to DC5: estimated from deepest seven samples from DC2 to DC4, averaged with all samples from DC5.

<sup>b</sup>LOI, loss on ignition determined as 100 – (sum total wt% oxides from lithium metaborate fusion analysis by ICP-AES).

<sup>c</sup>Parent composition for DC1 included for comparison: estimated from five of six deepest DC1 samples, i.e. excluding bottom-most sample (Jin *et al.*, 2010).

Elemental concentrations for DC3 samples from borehole CZMW2 Table II.

Sample ID	Depth (m BLS)	Al (wt%)	Ca (wt%)	Fe (wt%)	K (wt%)	Mg (wt%)	Mn (wt%)	Na (wt%)	P (wt%)	Si (wt%)	Ti (wt%)	Zr (ppm)	Total carbon <sup>d</sup> (wt%)	LOI <sup>b</sup> (wt%)
DC3 0-1	-0.15	8.3	0.52	4.19	2.16	0.54	0.155	0.34	0.03	29.2	0.55	280	1.87	9.6
DC3 1-2	-0.46	10.2	0.39	6.20	3.33	0.74	0.031	0.26	0.03	27.1	0.55	225	0.44	6.5
DC3 2-3	92.0-	6.7	0.35	5.25	3.32	0.73	0.101	0.31	0.03	28.9	0.58	290	0.22	4.9
DC3 3-4	-1.07	10.5	0.32	5.58	3.64	0.78	0.132	0.26	0.05	27.1	0.58	230	0.26	6.3
DC3 4-5	-1.37	10.6	0.29	5.71	3.74	0.80	0.085	0.24	90.0	27.0	0.59	225	0.22	0.9
DC3 5-6	-1.68	10.6	0.27	5.78	3.67	0.82	0.085	0.24	0.04	27.8	0.59	230	0.13	4.5
DC3 7-8	-2.29	6.6	1.84	7.98	3.18	0.88	0.349	0.22	0.14	23.8	0.53	175	0.58	8.9
DC3 8-9	-2.59	10.7	1.21	6.63	3.59	0.88	0.194	0.27	0.10	24.5	0.56	175	0.45	8.5
DC3 12-13	-3.81	10.3	0.58	5.56	3.52	98.0	0.147	0.27	0.07	27.1	0.58	245	0.26	6.4
DC3 21-22	-6.55	9.8	86.9	6.27	2.88	0.91	0.170	0.22	0.07	21.2	0.47	185	2.25	13.0
DC3 22-23	98-9-	10.5	1.69	2.66	3.72	0.92	0.085	0.27	0.065	25.7	0.57	195	0.62	7.0
DC3 27-28	-8.38	11.4	1.29	5.40	4.10	1.16	0.070	0.30	0.061	26.2	0.58	160	0.61	4.4
DC3 32-33	-9.91	11.2	1.51	5.36	4.01	1.12	0.062	0.32	0.022	26.0	0.58	165	0.65	5.0
DC3 37-38	-11.43	11.2	1.13	5.41	4.10	1.16	0.062	0.30	0.057	25.8	0.58	140	0.54	5.8
DC3 42-43	-12.96	10.6	1.49	5.70	3.79	1.22	0.070	0.27	0.035	26.1	0.57	175	0.7	5.5
DC3 47-48	-14.48	11.2	1.16	5.54	3.96	1.16	0.062	0.28	0.052	25.8	0.59	165	0.59	5.6
DC3 52-53	-16.01	10.6	0.51	5.69	3.70	0.97	0.101	0.33	0.039	27.9	0.64	315	0.28	3.4
Parent <sup>a</sup>		10.9	1.09	5.57	3.90	1.14	90.0	0.30	0.04	26.4	0.59	183		
Standard deviation.		0.4	0.42	0.24	0.20	0.07	0.02	0.02	0.02	0.7	0.03	35		
Parent DC1 <sup>c</sup>		10.7	0.17	5.49	3.83	1.06	0.07	0.34	0.05	26.7	0.61	171		
Standard-deviation		9.0	0.01	0.31	0.22	60.0	0.02	0.03	0.00	0.4	0.04	16		

Parent for DC2 to DC5: estimated from deepest seven samples from DC2 to DC4, averaged with all samples from DC5.

<sup>b</sup>LOI, loss on ignition, here LOI = 100 – sum total wt% oxides from lithium metaborate fusion analysis by ICP-AES.

<sup>c</sup>Parent composition for DC1 included for comparison: estimated from five of the six deepest DC1 samples (Jin *et al.*, 2010), i.e. excluding bottom-most sample.

<sup>d</sup>Total carbon (organic + inorganic) determined using elemental analyzer as described in text.

Elemental concentrations for DC4 samples from borehole CZMW3 Table III.

Sample ID	Depth (m BLS)	Al (wt%)	Ca (wt%)	Fe (wt%)	K (wt%)	Mg (wt%)	Mn (wt%)	Na (wt%)	P (wt%)	Si (wt%)	Ti (wt%)	Zr (ppm)	LOI <sup>b</sup> (wt%)
DC4 0-1	-0.15	10.2	0.34	5.46	3.246	0.73	0.077	0.27	0.03	28.4	0.58	245	4.9
DC4 1-2	-0.46	8.8	0.35	4.87	2.897	99.0	0.050	0.39	0.02	30.7	0.58	330	3.9
DC4 2-3	-0.76	10.2	0.30	2.90	3.528	92.0	0.070	0.28	0.04	28.5	0.61	245	3.7
DC4 3-4	-1.07	8.9	0.36	5.40	2.847	0.62	0.050	0.33	0.05	29.7	0.65	320	5.1
DC4 4-5	-1.37	8.6	0.35	6.64	3.08	0.64	060.0	0.31	0.05	28.4	99.0	270	4.1
DC4 6-7	-1.98	10.1	0.31	6.03	3.445	0.73	0.100	0.28	0.04	28.0	0.63	240	4.7
DC4 14-15	-4.42	10.6	1.36	5.39	3.711	0.89	0.100	0.30	0.05	26.7	0.58	210	5.5
DC4 19-20	-5.95	9.3	98.9	5.96	3.213	0.92	0.210	0.26	90.0	21.5	0.49	165	11.3
DC4 24-25	-7.47	11.0	1.37	5.56	3.893	1.19	060.0	0.32	0.03	26.2	0.58	180	2
DC4 29-30	-8.99	11.4	0.79	5.80	4.101	1.14	0.046	0.31	0.04	26.0	0.59	150	4.9
DC4 34-35	-10.5	11.1	0.94	5.64	3.952	1.07	0.039	0.28	0.08	26.3	09.0	175	2
DC4 39-40	-12.04	11.5	0.39	5.79	4.126	1.19	0.031	0.27	0.07	26.5	0.61	155	4.1
DC4 44-45	-13.6	11.3	0.59	5.45	4.134	1.15	0.046	0.30	0.03	27.0	0.61	180	3.7
DC4 49-50	-15·1	10.1	0.81	5.42	3.595	1.15	0.054	0.27	0.03	27.5	09.0	215	5.3
DC4 54-55	-16.6	10.4	0.91	5.45	3.777	1.13	0.054	0.27	0.03	27.0	0.59	190	5.2
Parent <sup>a</sup>		10.9	1.09	5.57	3.90	1.14	90.0	0.30	0.04	26.4	0.59	183	
Standard deviation		0.4	0.42	0.24	0.20	0.07	0.02	0.02	0.02	0.7	0.03	35	
Parent DC1 <sup>c</sup>		10.7	0.17	5.49	3.83	1.06	0.07	0.34	0.05	26.7	0.61	171	
Standard deviation ·		9.0	0.01	0.31	0.22	60.0	0.02	0.03	0.00	0.4	0.04	16	

<sup>a</sup>Parent for DC2 to DC5: estimated from deepest seven samples from DC2 to DC4, averaged with all samples from DC5. <sup>b</sup>LOI, loss on ignition, here LOI = 100 - sum total wt% oxides from lithium metaborate fusion analysis by ICP-AES. <sup>c</sup>Parent composition for DC1 included for comparison: estimated from five of the six deepest DC1 samples (Jin et al., 2010), i.e. excluding bottom-most sample.

 Table IV.
 Elemental concentrations for DC5 samples from borehole CZMW4

Sample	Depth (m BLS)	AI (wt%)	Ca (wt%)	Fe (wt%)	K (wt%)	Mg (wt%)	Mn (wt%)	Na (wt%)	P (wt%)	Si (wt%)	Ti (wt%)	Zr (ppm)	LOI <sup>b</sup> (wt%)
DC5 5 31-32	-9.5	10.3	1.86	2.66	3.66	1.21	0.11	0.27	0.052	25.4	0.56	170	7.3
DC5 36-37	-11-1	10.5	1.48	5.23	3.84	1.16	0.08	0.28	0.057	26.0	0.58	170	9.9
DC5 41-42	-12.6	10.7	1.09	5.17	3.92	1.13	0.07	0.28	0.013	26.3	0.58	175	6.3
DC5 47-48	-14.4	11.4	0.74	5.29	4.19	1.15	0.02	0.31	0.065	26.2	0.59	145	5.1
DC5 52-53	-15.9	11.2	96.0	5.19	4.04	1.18	0.02	0.33	pq	25.9	0.61	165	6.1
Parent <sup>a</sup>		10.9	1.09	5.57	3.90	1.14	90.0	0.30	0.04	26.4	0.59	183	
Standard deviation		0.4	0.42	0.24	0.20	0.07	0.02	0.02	0.02	0.7	0.03	35	
Parent DC1 <sup>c</sup>		10.7	0.17	5.49	3.83	1.06	0.07	0.34	0.05	26.7	0.61	171	
Standard deviation		9.0	0.01	0.31	0.22	60.0	0.02	0.03	0.00	0.4	0.04	16	

Parent composition for DC1 included for comparison: estimated from five of the six deepest DC1 samples (Jin et al., 2010), i-e., excluding bottom-most sample Parent for DC2 to DC5: estimated from deepest seven samples from DC2 to DC4, averaged with all samples from DC5. <sup>b</sup>LOI, loss on ignition, here LOI = 100 – sum total wt% oxides from lithium metaborate fusion analysis by ICP-AES.

Elemental concentrations (wt%) 0.01 0.1 100 2 4 6 Depth (m) 10 12 14 Ca - Mg 16 -□- Na -0- Si 18

**Figure 2.** Major element concentrations, measured from cuttings from the CZMW2 borehole (DC3 samples), plotted versus depth (in m BLS). High calcium (Ca) concentrations are observed at 2·4 and 6·2 m depth BLS but Ca concentrations above 2 m are almost  $10 \times$  lower than samples at depth (see Table II). Aluminum (AI), iron (Fe), magnesium (Mg), sodium (Na), and silicon (Si) remain relatively constant with depth compared to Ca.

were reproducible at this level. The accuracy of analysis of Cody shale was observed to equal  $\pm 1\%$ . In contrast, for the soil/sediment standards, the relative accuracy decreases from  $\pm 7\%$  (at 2.4 wt% Fe²+) to  $\pm 25\%$  (at 0.96 wt% Fe²+) to 35% (at 0.59 wt% Fe²+). Lower accuracy in the sediment/soil samples is likely due to the small Fe²+ content and interferences from the organic matter.

Long-term reproducibility of sulfur analysis on the LECO standard was  $\pm 26\%$  and accuracy was  $\pm 15\%$  (Table VII). The analysis completed on soil sample LGW1 by our laboratory reproduced the value measured at LECO, Inc.

The only sulfur-containing mineral we have observed in SSHO rocks and soils is pyrite (Figure 3) (Jin *et al.*, 2011b). For example, pyrite was observed to be present as framboids in polished sections under scanning electron microscopy from DC1-38 at 24·5 m depth (not shown) and μ-CT imaging from DC1-9 at 1·3 m depth (Figure 3D). The total sulfur concentrations were therefore attributed to pyrite. As shown in Figure 4, sulfur (pyrite) was depleted above 8 m depth in DC3 samples from the valley (Table VII). Pyrite was also depleted above 23 m depth in DC1 at the ridge (Table VII). Likewise, Fe<sup>2+</sup> was significantly depleted above about 7 m in DC3 samples (Table VI, Figure 5) and above about 20 m in DC1 (Table VI).

On a molar basis, however, the loss of sulfur is minor compared to the total loss of ferrous iron in DC3 samples (Tables VI and VII). Therefore, significant oxidation of ferrous iron in illite, chlorite, and possibly ankerite has also

**Table V.** Values of  $\tau_{Zr,j}$  for borehole CZMW2 (DC3<sup>a</sup> samples)

Sample ID	Depth (m BLS)	Al	Ca	Fe	K	Mg	Mn	Na	Р	Si
DC3 0-1	<b>−</b> 0·15	-0.50	-0.69	-0.51	-0.64	-0.69	0.57	-0.25	-0.54	-0.28
DC3 1-2	-0.46	-0.24	-0.71	-0.10	-0.31	-0.47	-0.61	-0.29	-0.51	-0.17
DC3 2-3	-0.76	-0.44	-0.80	-0.41	-0.46	-0.59	-0.01	-0.34	-0.49	-0.31
DC3 3-4	-1.07	-0.24	-0.77	-0.20	-0.26	-0.45	0.63	-0.30	-0.12	-0.19
DC3 4-5	-1.37	-0.21	-0.78	-0.17	-0.22	-0.43	0.08	-0.33	0.06	-0.17
DC3 5-6	-1.68	-0.23	-0.80	-0.18	-0.25	-0.43	0.05	-0.36	-0.20	-0.17
DC3 7-8	-2.29	-0.05	0.76	0.50	-0.15	-0.19	4.65	-0.22	2.46	-0.06
DC3 8-9	-2.59	0.02	0.16	0.24	-0.04	-0.20	2.14	-0.06	1.41	-0.03
DC3 12-13	-3.81	-0.30	-0.60	-0.26	-0.33	-0.43	0.71	-0.31	0.12	-0.24
DC3 21-22	-6.55	-0.22	5.34	0.11	-0.27	-0.21	1.62	-0.26	0.59	-0.21
DC3 22-23	-6.86	-0.10	0.46	-0.05	-0.11	-0.24	0.24	-0.16	0.41	-0.09
DC3 27-28	-8.38	0.19	0.35	0.11	0.20	0.17	0.24	0.14	0.60	0.13
DC3 32-33	<b>-</b> 9⋅91	0.14	0.54	0.07	0.14	0.09	0.07	0.19	-0.44	0.09
DC3 37-38	-11.43	0.34	0.36	0.27	0.37	0.33	0.26	0.34	0.70	0.27
DC3 42-43	-12.96	0.02	0.43	0.07	0.02	0.12	0.13	-0.06	-0.16	0.03
DC3 47-48	-14.48	0.14	0.18	0.10	0.12	0.13	0.07	0.05	0.33	0.08
DC3 52-53	-16.01	-0.43	-0.73	-0.41	-0.45	-0.51	-0.09	-0.35	-0.48	-0.39

<sup>&</sup>lt;sup>a</sup>Parent concentration summarized in Table II.

Table VI. Iron concentrations for DC1 and DC3 samples

Sample ID	Depth inter	val (m BLS)	Fe <sub>Total</sub> (wt% Fe)	Fe <sup>2+</sup> (wt% Fe)	Fe <sup>3+</sup> (wt% Fe)	Measured (wt% Fe <sup>2+</sup> ) <sup>a</sup>	USGS reported (wt% Fe <sup>2+</sup> )
DC3 2-3	-0.61	-0.91	5.52	0.97	4.54		
DC3 4-5	-1.22	-1.52	6.06	1.15	4.91		
DC3 7-8	-2.13	-2.44	7.24	1.42	5.82		
DC3 12-13	-3.66	-3.96	5.94	2.19	3.74		
DC3 21-22	-6.40	-6.71	7.20	3.52	3.68		
DC3 22-23	-6.71	-7.01	6.08	2.87	3.21		
DC3 27-28	-8.23	-8.53	5.64	4.94	0.70		
DC3 32-33	-9.75	-10.10	5.64	4.74	0.89		
DC3 37-38	-11.30	-11.60	5.74	4.66	1.07		
DC3 42-43	-12.80	-13.10	6.02	5.44	0.59		
DC3 47-48	-14.30	-14.60	5.87	4.90	0.97		
DC3 52-53	-15.80	-16.20	5.88	3.79	2.09		
DC1-4 <sup>b</sup>	-0.49	-0.61	5.36	1.28	4.08		
DC1-8 <sup>b</sup>	-1.10	-1.22	5.44	1.24	4.20		
DC1-11 <sup>b</sup>	-1.52	-1.71	5.60	1.33	4.27		
DC1-17 <sup>b</sup>	-3.35	-3.54	5.46	1.34	4.12		
DC1-23 <sup>b</sup>	-5.18	-5.36	5.26	1.23	4.03		
DC1-26 <sup>b</sup>	<b>-6</b> ⋅10	-6.28	5.97	1.10	4.87		
DC1-29 <sup>b</sup>	-10.67	-10.85	5.67	1.10	4.57		
DC1-35 <sup>b</sup>	-19.81	-19.99	5.36	2.34	3.02		
DC1-37 <sup>b</sup>	-22.86	-23.04	5.20	3.67	1.53		
References							
SCO-1						$0.69 \ (\pm 0.02, \ n = 6)$	0.70
MAG						$2.22 (\pm 0.12, n = 5)$	2.38
GXR2						$0.80 \ (\pm 0.04, \ n = 2)$	0.60
GXR5						$1.19 (\pm 0.10, n = 4)$	0.96

<sup>&</sup>lt;sup>a</sup>All references are from USGS. SCO-1 was run interspersed with DC sample analyses. Samples MAG (marine sediment), GXR2 (soil), and GXR5 (soil) were run over many days using the same method but not interspersed with DC samples. Based on all analyses for all standards, the relative reproducibility is  $\pm 10\%$ , but the accuracy and reproducibility for SCO-1, a sample of Cody shale, are  $\pm 1\%$  and 3% respectively. Relative accuracy increases from  $\pm 7\%$  (at  $2\cdot 4$  wt% Fe) to  $\pm 25\%$  (at  $1\cdot 2$  wt% Fe) to 35% (at  $0\cdot 59$  wt% Fe) for the sediment/soil samples due to the presence of organic matter and low iron content. Based on these measurements, we estimate that accuracy of samples of core are approximately  $\pm 5\%$  and regolith vary in the range  $\pm 5-35\%$ .

occurred in DC3 samples. In contrast to the valley floor boreholes, however, significant ferrous iron is still present in the DC1 cuttings above the pyrite front, presumably in the remaining chlorite and illite. Apparently, chlorite/illite is oxidized above the pyrite depletion zone at the valley floor but not in the ridge.

#### μ-CT observations

Although little sulfur is left in DC1 samples above 22 m (Table VII), some samples were occasionally observed under  $\mu$ -CT to retain a few high density aggregates identified as pyrite framboids (e.g. sample DC1-9 from 1·22 to 1·40 m depth,

<sup>&</sup>lt;sup>b</sup>Analyses reported by Jin et al. (2011b).

**Table VII.** Values of *R* and concentrations of sulfur and pyrite in DC1 and DC3

Sample <sup>a</sup>	Depth (m)	wt. % Sulfur	wt. % Pyrite	$R^{\rm b}$
DC3 1-2	-0.46	0.0063	0.013	
DC3 3-4	-1.07	0.0058	0.012	
DC3 7-8	-2.29	0.0069	0.014	
DC3 12-13	-3.81	0.0056	0.011	
DC3 21-22	-6.55	0.0068	0.014	
DC3 27-28	-8.38	0.0906	0.181	0.11
DC3 32-33	-9.91	0.0981	0.196	0.13
DC3 37-38	-11.43	0.1140	0.228	0.18
DC3 42-43 <sup>a</sup>	-12.96	0.1101	0.220	0.18
DC3 42-43 <sup>b</sup>	-12.96	0.1170	0.234	
DC3 47-48	-14.48	0.0822	0.164	0.15
DC3 52-53 <sup>a</sup>	-16.01	0.0891	0.178	0.32
DC3 52-53 <sup>b</sup>	-16.01	0.0903	0.181	
DC3 52-53 <sup>c</sup>	-16.01	0.0857	0.171	
DC1-17	-3.4	0.009	0.017	
DC1-20	-4.4	0.006	0.011	
DC1-29	-10.8	0.003	0.006	
DC1-32	-15.3	0.006	0.012	
DC1-37	-23.0	0.144	0.270	0.45
DC1-38	-24.5	0.121	0.227	0.07
LGW1 85 <sup>c</sup>		0.034		
LGW1 85 <sup>d</sup>		0.035-0.038		
Standard <sup>d</sup>		0.0288		
Standard <sup>e</sup>		$0.0246 \pm 0.006$	54	

<sup>&</sup>lt;sup>a</sup>Samples that were split and analyzed multiple times to determine reproducibility are indicated by a, b, c.

Figure 3D). Pyrite was commonly observed using μ-CT at depths below 20 m where the sulfur concentration increased (e.g. DC1-36 sample from approximately 21-3 to 21-5 m depth, Figure 3A). The CT imaging also revealed that porosity had developed around some of the pyrite grains in that sample (see Figure 3A image and compare images Figures 3B and 3C). Specifically, the µ-CT images were thresholded to distinguish pores and grains (Figure 3A) or to distinguish the high-density material presumed to be pyrite (Figure 3B). With each of these threshold values, the skeleton was calculated. The skeleton is a representation that shows the general shape of an object (in this case the pyrite or pore distribution). Comparison of the skeletons in Figures 3A and 3B emphasizes that pores were commonly detected around the pyrite grains. Importantly, the sample imaged in Figure 3 only had 1.07% porosity as measured by the  $\mu$ -CT, documenting that porosity-initiating reactions were occurring around the pyrite in rock sections even when overall porosity was very low (note that μ-CT does not resolve submicron pores).

#### XRD and carbon data

Table VIII summarizes mineral concentrations for DC3 samples (from CZMW2). Quartz is generally constant with depth and illite is present at all depths as the dominant clay, varying from 43 to 57 wt%. As the second most abundant clay, 'chlorite' (a term used here to indicate chlorite + vermiculite + hydroxyl interlayered vermiculite (HIV), none of which were distinguished separately in the XRD and RockJock analyses reported here) was

also observed in the profile except in the shallowest sample. Kaolinite was detectable at depths of 1.6 m and above.

The carbonate minerals ankerite and calcite also show variability in abundance based on XRD data (Table VIII). These RockJock-calculated abundances are relatively accurate only for minerals at higher abundance and we therefore summed the estimated concentrations from XRD for the carbonate minerals in Table VIII. The two spikes in calcium concentrations at depths of  $2 \cdot 1 - 2 \cdot 3$  and  $6 \cdot 2 - 6 \cdot 4$  m in DC3 samples (Figures 2 and 6) correlate with higher (calcite + ankerite) concentrations. For example, the highest calcium concentration (at about  $6 \cdot 5$  m depth) in DC3 coincides with the highest percent (calcite + ankerite) (Table VIII), the highest LOI (Table II), and the highest wt% total carbon (Table II). Recasting the total carbon at that depth as wt% calcite yields  $18 \cdot 8$  wt% calcite which compares favorably to the XRD-determined value of  $17 \cdot 7$  wt% (calcite + ankerite).

At first glance, the lack of calcite + ankerite above about 2 m in DC3 may appear inconsistent with the total carbon data in Table II. However, wt% total carbon is lowest at about 1.7 m depth: higher values at deeper depths are likely (calcite + ankerite) while higher values at shallower depths are likely organic carbon. Consistent with the presence of organic carbon in the shallow samples, the  $\delta^{13}$ C of three of these samples range from -25 to -33% (Table IX), as expected for modern  $C_3$ organic matter (Vogel, 1993). In contrast, beneath 2 m in DC3 samples and for the two samples in DC1,  $\delta^{13}$ C values range between -10 and -15%. Only one sample from the layer of highly concentrated carbonate at 6.7 m showed a distinctly different value (-2.9%) in DC3 samples. This sample is hypothesized to represent relatively recently precipitated secondary carbonate rather than primary carbonate from the original shale.

#### Water table

Measured depths to the water table in well 4 (Figure 1), the closest groundwater well to the CZMW boreholes, varied from approximately 0.6 to 1.4 m BLS (Table X). During the winter and fall when water flows in the stream, the water table rises to zero meters or above. Therefore, in 2010 the water table at the valley floor fluctuated by only about a meter from the driest to wettest months. In contrast, as measured in well DC0 at the ridge, the winter water table was at 19–20 m depth BLS but during summer it was at 26 m BLS.

# Discussion

#### The upper fractured layer

Jin et al. (2010) showed that under the northern ridge, an upper ~5 or 6 m-thick layer is distinct from deeper layers in elemental content and density. One sample from DC1 taken from 4.5 m depth was particularly anomalous in that it had high LOI and iron content. The uppermost part of the 5–6 m layer can be observed in pits to consist of blades of rock — tens of centimeters in length/width and centimeters in thickness – interspersed with minor silt, sand, and clay. Much of the character of this upper 5–6 m was attributed by Jin et al. (2010) to fracturing driven by freeze—thaw (Murton et al., 2006; Matsuoka and Murton, 2008) that has been ongoing since at least the peri-glacial conditions 15 000 year before present (Gardner et al., 1991).

In addition to the large-scale fracturing that produced the bladed shale beneath the regolith, rock fragments recovered during drilling from the 5–6 m layer vary greatly with respect

<sup>&</sup>lt;sup>b</sup>From Equation 7 in text.

<sup>&</sup>lt;sup>c</sup>Sample of Puerto Rico quartz diorite from the Luquillo Critical Zone Observatory analyzed in our laboratory.

<sup>&</sup>lt;sup>d</sup>Value for Puerto Rico quartz diorite sample as reported by LECO.

<sup>&</sup>lt;sup>e</sup>Long-term average measurement  $(\pm 1\sigma)$  of the LECO standard in our laboratory (n = 18).

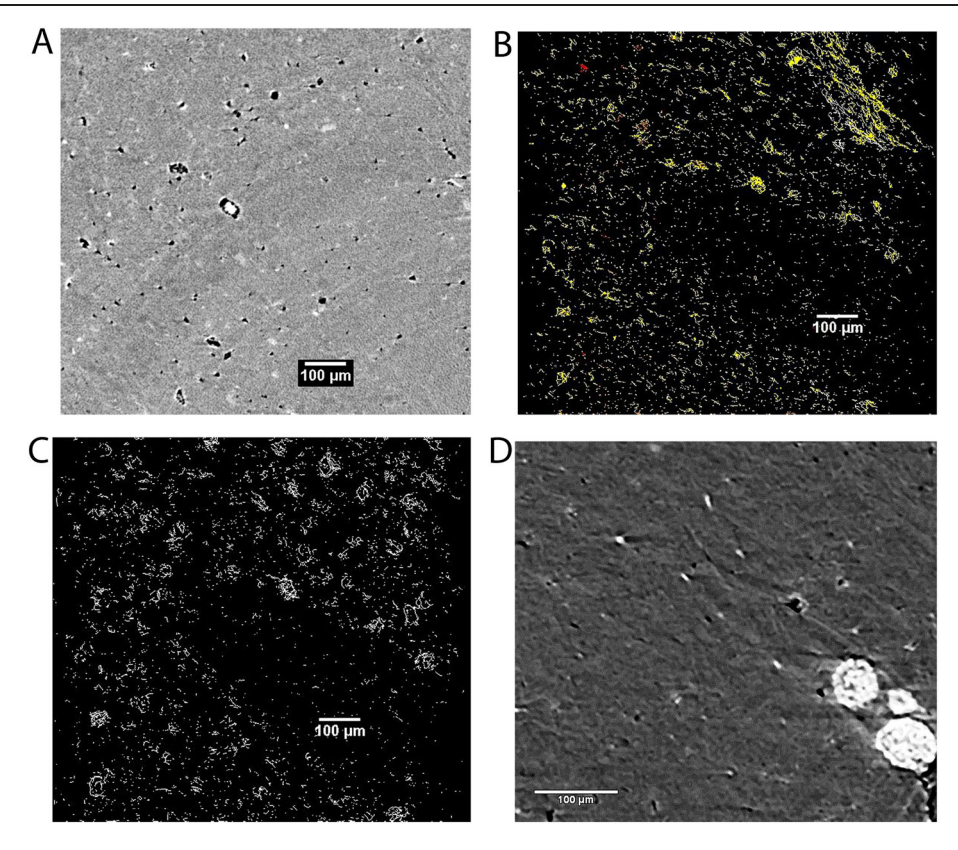
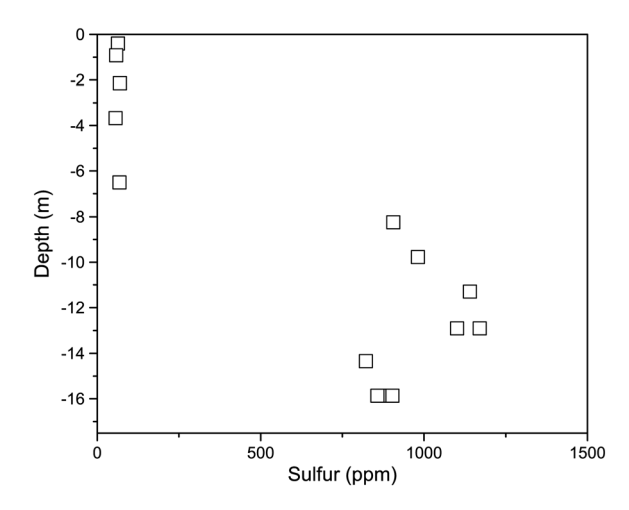
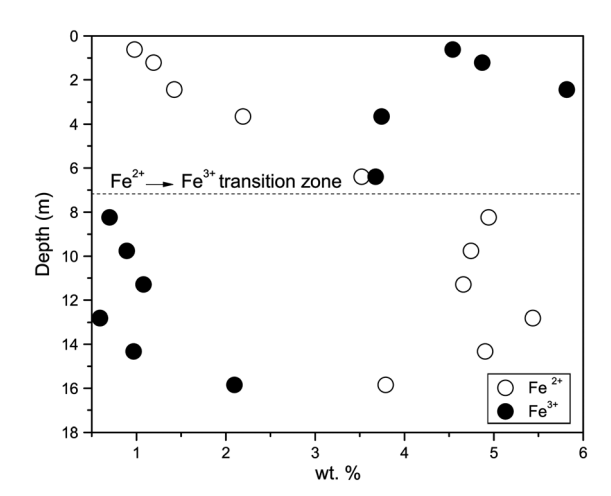


Figure 3. (A) μ-CT image of a shale fragment from DC1-36 from DC1 borehole from 21.3 to 21.5 m depth. The sample was imaged in 250 images which were 1.8 μm thick each and one slice is shown here. Dark gray to black areas are pores and extremely bright white areas are high density material, inferred to be pyrite. One pore in the center left is partly filled with high density material. Porosity around the pyrite is attributed to oxidative dissolution. Total porosity measurable by μ-CT for the subsample  $(0.38 \text{ mm}^3)$  is  $1.07 \pm 0.03\%$ . The image was collected at 1.7 μm/pixel resolution, i.e. the minimum pore that can be imaged has dimension equal to about 5 μm. (B) The stack of 250 μ-CT slices collected for the sample in A were analyzed together and thresholded for calculation of pores. The skeleton image of the thresholded pores shown here indicates pores (yellow) that appear both largely unconnected (for example, especially in lower left region) and connected (e.g. upper right side of the image). (C) The same stack of images used for B were thresholded here for the high density material (see Figure 3A for description). The calculated skeleton is shown here. Some round white objects are located at the same place as pores shown in Figure 3B, which indicates this white dense material (presumed to be pyrite) spatially connects with pores. (D) μ-CT image of sample DC1-9 from 1·22 to 1·40 m depth. The high density material clearly exhibits the geometry of pyrite framboids (bright raspberry-like objects in bottom right). Image resolution is 0·9 μm/pixel, i.e. smallest detectable diameter of a feature is ~3 μm. Note that this sample is from the unsaturated zone where most pyrite has already been oxidized. This figure is available in colour online at wileyonlinelibrary.com/journal/espl



**Figure 4.** Sulfur concentration (Table VII) plotted versus depth BLS for DC3 samples from CZMW2. Pyrite is the only sulfur-containing mineral identified in the rocks. Sulfur is depleted from 0 to 7 m depth but present beneath that depth.

to bulk density even though they do not contain visible microfractures (Jin *et al.*, 2011b). Some of this porosity can be attributed to loss of base cations: for example, loss of sodium was noted by Jin *et al.* (2010, 2011b) and attributed to the



**Figure 5.** Plots of wt%  $Fe^{2+}$  or  $Fe^{3+}$  versus depth for DC3 samples from CZMW2 borehole. Samples were analyzed for total iron and  $Fe^{2+}$ , and  $Fe^{3+}$  was calculated by subtraction (Table VI). The iron titration data plotted here reveal a transition from predominantly ferrous to ferric iron at a depth of ~7 m, coincident with the transition from no pyrite to pyrite shown in Figure 4.

onset of weathering of minor feldspar down to several meters depth. However Jin *et al.* (2011b) argued that chemical losses are not extensive enough (e.g. Figure 7) to explain the lower

**Table VIII.** Quantitative mineralogy for DC3 samples<sup>a</sup>

Sample ID	Qz (wt%)	Kspar (wt%)	Plagioclase (wt%)	Cc + Ank (wt%)	Kao (wt%)	III (wt%)	Chlor + Vermi (wt%)
DC3 0-1	29.0	2.1	3.2	0.6	_	55.3	2.3
DC3 1-2	30.9	2.3	2.4	bd	1.9	43.5	11.3
DC3 2-3	36.2	4.5		0.4	0.8	50.6	9.4
DC3 3-4	29.1	4.9	1.8	0.1	0.6	54.9	11.5
DC3 4-5	25.8	2.7	1.7	1.2	1.2	57.2	6.2
DC3 5-6	29.0	2.1	0.9	0.6	_	55.3	11.8
DC3 7-8	24.1	2.5	1.1	4.0	_	49.7	14.0
DC3 8-9	24.2	2.4	0.6	2.6	0.1	53.0	13.9
DC3 12-13	30.3	2.1	1.1	1.1	0.7	53.5	11.4
DC3 21-22	24.2	1.3	1.1	17.3	_	42.5	12.2
DC3 22-23	26.1	3.5	0.8	3.6	0.1	12.6	12.6
DC3 27-28	25.0	3.1	bd	4.2	_	54.1	13.5
DC3 32-33	25.3	2.4	0.8	3.9	_	53.1	14.2
DC3 37-38	25.5	3.6	0.9	3.1	_	50.4	4.5
DC3 42-43	26.3	3.1	0.2	3.1	_	47.5	9.1
DC3 47-48	27.7	3.0	1.6	2.8	_	49.3	10.6
DC3 52-53	30.1	3.3	0.9	1.4	_	43.9	14.2

<sup>a</sup>All weight percents were normalized to 100, as determined using RockJock (USGS) following the protocol reported in Eberl (2009). Pyrite (or other minerals) detected in some samples at levels between 0·1 to 0·3 wt% are not reported here because these low values were not considered accurate in RockJock· Mineral codes as follows: Qz (quartz), Kspar (potassium feldspar), Cc (calcite), Ank (ankerite), Kao (kaolinite), Ill (illite), Chlor (chlorite), Vermi (vermiculite).

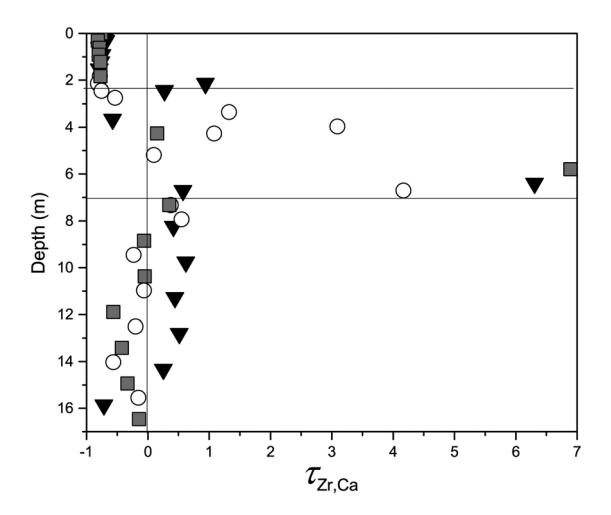


**Figure 6.** Plots of  $\tau_{Zr,Ca}$  versus depth for data from DC2, DC3, and DC4 samples from boreholes CZMW1 (open circles), CZMW2 (filled triangles) and CZMW3 (filled squares) respectively. Parent composition was assumed equal to seven deepest samples from DC2, DC3, and DC4 averaged with all samples from DC5 (see Table II). Above 2 m, Ca concentrations are very small in all samples: this depletion is attributed to dissolution of carbonate in the unsaturated zone. Various degrees of Ca enrichment are seen in samples from all three sets of borehole cuttings over depths ranging from 3 to 7 m. Ca enrichment is attributed to carbonate minerals (calcite and ankerite, see Table VIII). Based on isotopic data (Table IX), at least some of the high carbon content at 6·5 m depth (DC3) is likely due to secondary carbonate precipitation. Depletion of Ca above 2 m is attributed to the dissolution of both primary and secondary carbonates.

bulk density of chips in the upper 6-m layer. Changes in bulk density were therefore attributed to loss of particles from inside the chips as well.

The 5 or 6 m-deep fractured layer under the ridge is similar to the 6 or 7 m-thick fast-drilling layer identified in the valley (Kuntz *et al.*, 2011). In this layer under the valley, fracturing was identified by Kuntz *et al.* (2011) to be spaced more densely. In addition, natural gamma ray emission was lower, as expected for material that had lost clay particles containing

**Table IX.** Carbon isotopic compositions and total carbon contents

Sample ID	Depth (m)	δ <sup>13</sup> C	Wt% carbon
DC3 0-1	0.15	-25.5	2.0
DC3 1-2	0.46	-28.0	0.5
DC3 4-5	1.37	-32.9	0.4
DC3 7-8	2.29	-10⋅4	0.7
DC3 21-22	6.55	-2.9	2.9
DC3 22-23	6.86	-10⋅0	0.8
DC3 47-48	14.48	–11⋅5	0.7
DC1 37	22.95	-14.3	0.3
DC1 38	24.50	-14.4	1.8
Standard <sup>a</sup>		-27.5	1.5

<sup>a</sup>Elemental low carbon soil, reported  $\delta^{13}C = -27 \cdot 46\% \pm 0.11$  relative to PDB;1·52  $\pm$  0·02 wt% carbon. All carbon analyses here include inorganic + organic carbon (i.e. total carbon).

potassium. Consistent with this interpretation, the chemical compositions summarized here also document possible evidence for depletion of magnesium, potassium, and silicon in the uppermost 5–6 m layer under the valley (Figures 8–10). To be conservative in the calculations of  $\tau_{Zr,j}$ , all calculations for Figures 8-10 were made using the same values for the parent material. However, bottom-most samples from two of the boreholes (DC2 samples from CZMW1, DC3 samples from CZMW2) appear discrepant in composition, possibly indicating a different parent composition or variation in the Zr content. If bottom-most samples had been excluded in calculating  $\tau$ , the evidence for depletion of potassium, magnesium, and silicaon would be stronger. Regardless, Figures 8-10 can be considered to be consistent with, although not proof of, variable extents of loss of feldspar or illite (K, Si) along with 'chlorite' (Mg, Si) in the uppermost 6-m fractured layer.

Regardless whether loss of clay is occurring through solubilization or particle transport, significant fluid flow must be moving through the fractured layer to cause clay depletion. In fact, the uppermost fractured layer is likely to be penetrated readily by infiltrating rainfall when regolith becomes saturated. For example, researchers have argued that during dry periods, hydrophobicity of the organic horizon precludes rainfall from infiltrating into the

2011 August 18, 1.43 2.73 1.24 1.15 2.02 .55 26.1 2011 March 18, 19.4 0.45 0.39 0.59 0.41 2011 February 18, 20.2 0.84 0.84 0.61 0.85 November 20, 2010 0.18 1.96 0.08 1.03 2.74 1.58 November 5, 2010 2.05 2.05 3.38 1.07 0.49 0.71 3.23 2.07 2.73 2010 October 22, 2.09 2.09 1.13 1.18 1.44 2.95 1.37 3.2 2.19 2.58 September 2, 2010 Depth to water table in SSHO (2010–2011) (meters below land surface) 0.85 2.1 1.36 1.21 2.01 2.05 1.62 3.2 2.47 3.39 2.89 1.64 1.74 August 11, 2010 1.01 2.15 1.43 1.28 2.17 20, 2010 1.2 0.7 3.56 May April 22, 2010 0.63 1.93 0.85 1.21 0.81 3.9 Table X. CZMW2  $\Box$ CZMW4 Well 

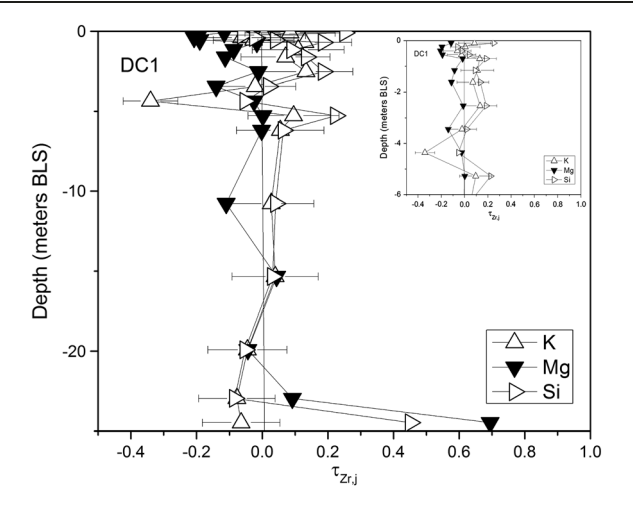


**Figure 7.** A plot of  $\tau_{Zr,j}$  versus depth (in m BLS) for DC1. Parent composition was defined equal to the average of samples from depths of five of the six deepest samples, without inclusion of the deepest sample which is known to contain significant ankerite (see parent composition summarized in Table I). Characteristic error bars were calculated and plotted for  $\tau_{Zr,K}$ . Error bars for other elements are similar in magnitude at each depth. The inset shows an expanded version of the upper part of the profile.

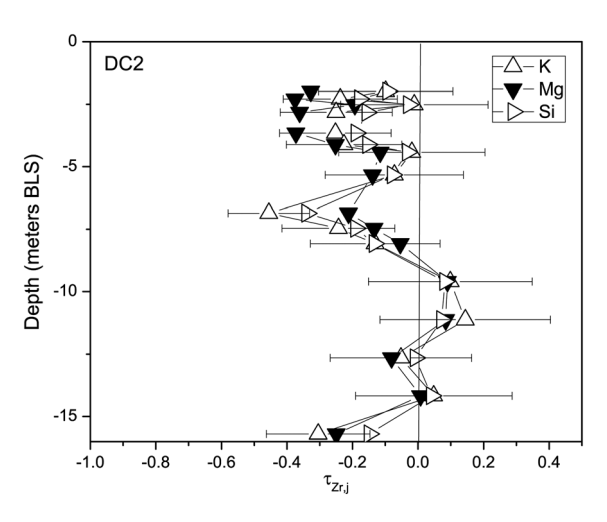


**Figure 8.** A plot of  $\tau_{Zr,j}$  versus depth (in m BLS) for DC2 samples from CZMW1. Parent composition was defined equal to the average of samples from the deepest seven samples from DC2, DC3, DC4 and all analyzed samples from DC5 (see Table I). Error bars were calculated and plotted for  $\tau_{Zr,K}$ . Error bars for other elements are similar in magnitude at each depth. Although the lowermost sample was used in the calculation for parent (to be conservative), it is nonetheless possible that this sample has intersected the next unit, Keefer sandstone.

soil homogeneously (Lin and Zhou, 2008). Instead, Lin and Zhou (2008) argued that the rain penetrates along vertical macropores directly into the underlying fractured bedrock. Whenever the fractured zone becomes saturated with fluid, these zones become intermittently perched layers. Along such perched layers, water will advect down the hillslopes above the regional water table. Such interflow has been identified at Shale Hills (Lin *et al.*, 2005; Jin *et al.*, 2011a). For example, the interface between the regolith that can be augered by hand – where hydraulic conductivities have been measured to equal  $10^{-9}$  to  $10^{-4}$  m/s – and the underlying shale where conductivities equal  $\sim 10^{-15}$  m/s, is a likely zone of interflow (Lin, 2006; Jin *et al.*, 2010, Jin *et al.*, 2011a; Kuntz *et al.*, 2011). In addition, the layer at 4-5 m depth in DC1 that

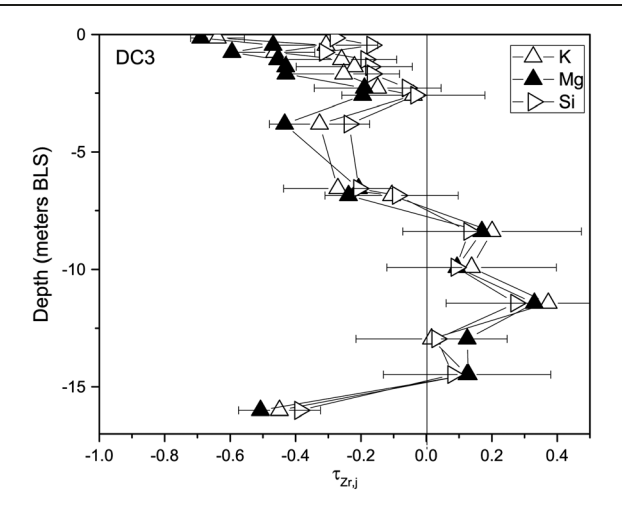


**Figure 9.** A plot of  $\tau_{Zr,J}$  versus depth (in m BLS) for DC3 samples from borehole CZMW2 using parent composition defined equal to the average of samples from the deepest seven samples from DC2, DC3, DC4 and all analyzed samples from DC5 (see Table II). Error bars were calculated and plotted for  $\tau_{Zr,K}$ . Error bars for other elements are similar in magnitude at each depth. Although the lowermost sample was used in the calculation for parent (to be conservative), it is nonetheless possible that this sample has intersected the next unit, Keefer sandstone.

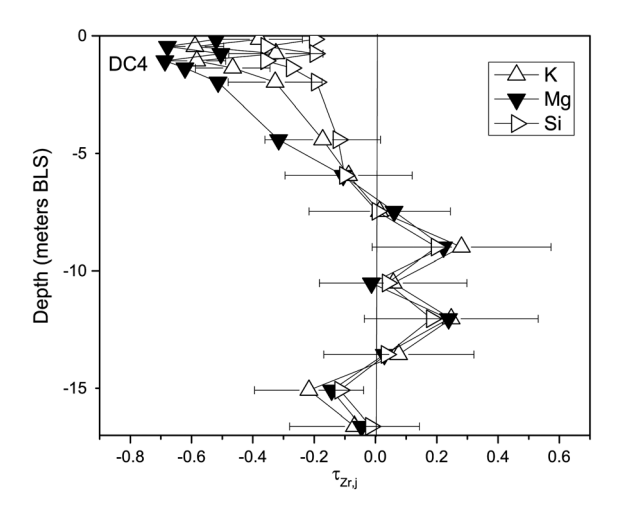


**Figure 10.** A plot of  $\tau_{Zr,j}$  versus depth (in m BLS) for DC4 samples from borehole CZMW3. Parent composition was defined equal to the average of the deepest seven samples from DC2, DC3, DC4 and all analyzed samples from DC5 (see Table III). Error bars were calculated and plotted for  $\tau_{Zr,K}$ . Error bars for other elements are similar in magnitude at each depth.

has anomalously high iron and LOI is likely a fracture that has served as a conduit of interflow that has precipitated iron oxyhydroxides.

Depletion of sodium, magnesium, potassium, and silicon never reaches 100% even in the regolith at the land surface: these feldspar and clay depletion profiles are therefore 'incompletely developed' profiles (Brantley and White, 2009; Jin *et al.*, 2010). On ridgetops, such incompletely developed profiles generally form where (i) erosion is slow and the duration of weathering is not long enough to completely deplete the soil; or (ii) the rate of erosion is fast compared to the rate of weathering of the phase of interest (Lebedeva *et al.*, 2010). The former case is essentially a transient in the evolution of regolith toward a steady state composition where regolith formation rate = erosion rate. The latter case is the case of kinetic-limited denudation where parameters

related to the mineral reaction rate are small compared to the erosion rate. For that case, any increase in the reaction rate of the mineral can increase the rate of total denudation. Such kinetic limitation is a likely explanation for the SSHO. This conclusion is consistent with the nature of shale in that it is easily eroded but only slowly dissolved.

#### Carbonate reaction front

As discussed in the Results section, concentrations of calcium or carbonates (calcite + ankerite) were insignificant above 2·1 m depth in all three valley boreholes as summarized in Table VIII and Figure 6. Some of the variation in carbonate is due to lithological heterogeneity in the Rose Hill formation (Flueckinger, 1969). It is undeniably difficult to identify a parent composition given the stratigraphic variations and the complexity of folding and faulting in the region. Given this highly folded and faulted nature, calcium content might be expected to be extremely variable in different locations.

However, calcium is not only insignificant above about 2 m depth in valley boreholes CZMW1, CZMW2, and CZMW3 (samples labeled DC2, DC3, and DC4) but also above 22 m in DC1 (ridge). Furthermore, these depths all roughly coincide with the measured regional water table (Table VIII, Figure 11). One interpretation is that the five boreholes intersect carbonate-rich layers fortuitously at the depths of the water table in both ridge and valley and that carbonates have never been present in strata above those depths even before weathering commenced. However, such a coincidence seems unlikely. Therefore, although the carbonate layers encountered beneath valley and ridge are most likely from different strata, the complete depletion of calcium-containing carbonates above the water table is more likely due to dissolution by CO2-charged fluids (or possibly sulfuric acid (H2SO4)charged fluids as discussed later) in the unsaturated zone (Figure 11).

According to this hypothesis, the variation of calcium concentrations with depth at the ridgetop can be thought of as a 'completely developed depletion profile' for carbonate (Brantley and White, 2009), i.e. carbonate minerals were originally present at variable concentrations but were 100% dissolved in the upper part of the profile. Completely developed profiles evolve for weathering under conditions known as local equilibrium. Indeed, at SSHO, the chemistry of the groundwater is high in calcium and magnesium concentrations compared to soil porewaters, consistent with equilibration at depth with carbonates (Jin et al., 2011a). A local equilibrium regime is expected for a mineral when the rate of erosion is slow in comparison to the mineral's dissolution rate. Since carbonates are fast-dissolving, they are usually expected to weather under local equilibrium (Lebedeva et al., 2010).

The calcium versus depth data can be interpreted as a carbonate depletion profile regardless of whether the carbonate is primary or secondary. Thus, even though the large change in carbon isotopic composition under the valley floor at ~6.6 m depth is consistent with precipitation of carbonate at that depth, such precipitation is not contradictory to the idea of a reaction front. Specifically, the upper 2 m are depleted in carbonate due to infiltration of fluids charged with  $\rm CO_2$  – and possibly organic acids – through the unsaturated zone. However, in fractures or layers beneath the water table, degassing of  $\rm CO_2$  (and low concentrations of organic acids) likely combines with increases in calcium concentration driven by pyrite-derived acids as described later to cause precipitation of carbonates instead of dissolution.

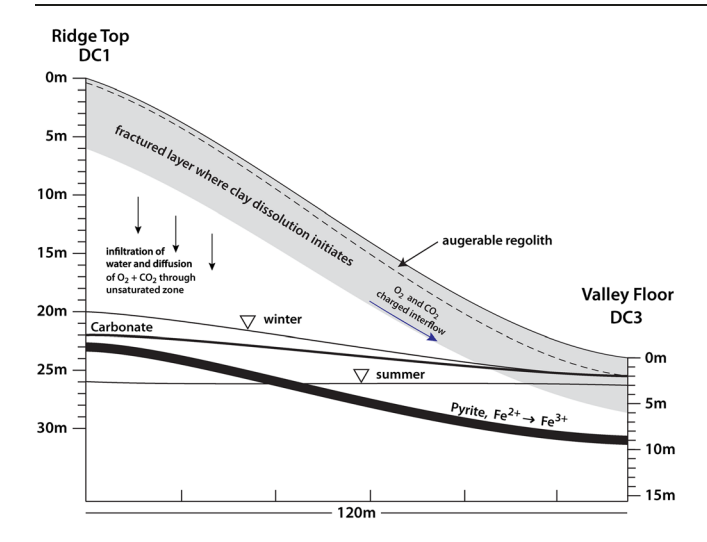


Figure 11. Nested geochemical reaction fronts are hypothesized to lie subparallel to the land surface under the Shale Hills catchment. In this schematic, the hypothesized fronts are plotted at the ridgetop (based on DC1 data) and the valley floor (based on DC2-DC5 samples from boreholes CZMW1-CZMW4), all projected to one cross-section across the catchment. The inferred reaction fronts are connected schematically. Inverted triangles indicate representative summer and winter water table depths (see Table X). Significant pyrite is not observed above 7 m depth in the valley floor, and above 23 m under the ridge. Significant carbonate is not observed above 2 m depth in the valley floor, and above 22 m under the ridge. We infer that carbonate and pyrite are both dissolved above these reaction fronts. Potassium and magnesium are observed in variable concentrations in the upper 6-7 m at ridge and valley, perhaps documenting loss of clay minerals as solutes or particles. This upper ~7 m-thick layer underlying the land surface is known to be highly fractured and less dense under both the ridge and valley. The layer is likely to host significant interflow downslope from ridge to valley (blue arrows). Under the ridge, diffusion of O2 to the pyrite oxidation front (black arrows) is fast because it is occurring through the unsaturated zone, explaining the rough coincidence of pyrite oxidation and the water table. Under both ridge and valley, O2 diffusion through the water-saturated zone is inferred to be slow. The position of the pyrite oxidation front beneath the water table at the valley is attributed to downslope advective transport of O<sub>2</sub> as oxygenated interflow waters. Degassing of CO<sub>2</sub> from interflow at the valley floor plus release of calcium to solution during carbonate dissolution driven by pyrite oxidation may cause significant precipitation of carbonate at ~7 m depth. This figure is available in colour online at wileyonlinelibrary.com/journal/espl

These interpretations for SSHO are not anomalous compared to other settings. Carbonate minerals are known to be more reactive and soluble than silicate minerals and they often weather first (MacDonald *et al.*, 1991; White *et al.*, 2005; Szramek *et al.*, 2007; Williams *et al.*, 2007). Given this high reactivity, carbonate minerals weather very rapidly from soil profiles where rainfall is plentiful and are almost always depleted from surface horizons even in extremely young and poorly developed soils (MacDonald *et al.*, 1991; Vandenbygaart and Protz, 1995; Lichter, 1998; Nezat *et al.*, 2007). Thus it is common for carbonate minerals to comprise completely developed depletion profiles in regolith on ridgetop locations where precipitation is greater on average than evapotranspiration.

#### Pyrite reaction front

Under the ridge, pyrite, like carbonate, comprises a completely developed depletion profile because it is only significant in concentration below 23 m depth. This depth roughly coincides

with the regional water table (Figure 11). The coincidence between pyrite depletion and the water table has been observed in other locations and attributed to rapid diffusion of  $O_2$  through gas-filled pores but slow diffusion through water-filled pores (Feng *et al.*, 2002). Of course, the depth of the water table moves up and down so exact correspondence between today's water table and pyrite depletion is not expected. In fact, the depth of depletion could document the deepest water table in the recent past that was maintained long enough to oxidize and remove pyrite.

It may seem mysterious how pyrite can dissolve in Rose Hill shale, given that porosities less than 5% have been reported in the bedrock and that most of the porosity in the unweathered rock is not connected (Jin *et al.*, 2011b). However, wherever  $O_2$  diffuses into the rock, oxidative dissolution of the pyrite will generate protons (e.g. Reaction 3). These protons may in turn dissolve more minerals to form new pores that allow infiltration of more gas and water. Indeed, Figures 3A–3C document that pores have formed around pyrite near the water table. Given the diffusion of  $O_2$  through the unsaturated zone, porefluids near the water table are likely to become acid due to pyrite oxidation while waters beneath the water table remain high in pH. Given the low porosity, some pyrite remains in the rock even above the water table (Figure 3D).

According to these arguments, downward diffusion of  $O_2$  through the unsaturated zone causes pyrite oxidation and the release of  $H_2SO_4$ , that opens the rock to further weathering. The first mineral that  $H_2SO_4$  is likely to dissolve is carbonate because of its high reactivity. This may partially explain why the putative pyrite and carbonate reaction fronts are close to one another (Figure 11). If carbonate is abundant and pyrite is not, very little porosity can be generated. However, if pyrite is abundant and carbonate is not, the porosity can grow. To assess this at SSHO, the acid generation capacity of samples (Rose and Cravotta, 1998) was calculated by noting that the moles  $CaCO_3$  that can be consumed are  $4\times$  the moles of pyrite oxidized:

$$FeS_2 + 3.75 O_2 + 3.5 H_2O + 4CaCO_3$$

$$= Fe(OH)_3 + 2 SO_4^{2-} + 4 Ca^{2+} + 4 HCO_3^{-}$$
(6)

We used Reaction 6 to define the acid-generating capacity *R* of the rock:

$$R = \frac{M_{pyr}}{4M_{CaCO_3}} \tag{7}$$

where  $M_{\rm pyr}$  and  $M_{\rm CaCO3}$  are the concentrations of pyrite and calcite in parent material (in mol/kg), respectively. If  $R \le 1$ , then oxidation of pyrite can cause dissolution of all or some fraction (= R) of the carbonate in the rock. Thus,  $O_2$ -charged fluids infiltrating such a rock are likely to produce  $H_2SO_4$  that is consumed during carbonate dissolution. In this case, the fronts of pyrite oxidation and carbonate dissolution are likely to be roughly coincident in location. If R > 1, then the fluids could carry the  $H_2SO_4$  from pyrite oxidation forward into the underlying rock, dissolving minerals other than calcite.

For Shale Hills below the putative carbonate front, R = 0.07 to 0.45 (Table VII). In other words, up to 45% of the carbonate dissolution under SSHO could have been due to pyritegenerated  $\rm H_2SO_4$ . However, the rock is not so pyrite-rich and carbonate-poor that  $\rm H_2SO_4$  is likely to have infiltrated outside the zone of pyrite reaction because the acid produced by

pyrite oxidation must have been buffered by carbonate dissolution. Given that R < 1,  $H_2SO_4$  likely dissolved some of the carbonate but some other acid such as  $CO_2$  that diffused throughout the unsaturated zone must have contributed to carbonate dissolution. Organic acids may also be important in upper soil layers where rates of organic production are faster than decomposition.

One final puzzle remains with respect to carbonate and pyrite distributions at Shale Hills: while pyrite oxidation under the ridge at SSHO is coincident with the water table, under the valley, pyrite has apparently oxidized deeper than today's water table where diffusive transport of O2 is known to be slow (Feng et al., 2002). One explanation might be that the loss of pyrite below the water table only occurred during previous time periods when the water table was much lower. However, given the rough coincidence of oxidation with the 6 m-thick fractured layer under the valley, we prefer the explanation that O2 is advected to the pyrite front under the valley by downslope interflow. Evidence for flow of oxidized fluids in the fractured layer is documented, for example, by the iron-rich layer at 4.5 m depth in DC1 that has anomalously high LOI. Coincidence between pyrite oxidation under the valley and carbonate precipitation could also point to coupled pyrite oxidation and carbonate precipitation such that the calcium for the calcite is derived from H<sub>2</sub>SO<sub>4</sub>-driven dissolution of Ca-containing silicates (Drake et al., 2009). These observations are summarized in Figure 11.

#### Patterns of deep weathering

While we cannot prove from only a few boreholes that chemical depth variations are due to nested reaction fronts instead of lithological variations, the idea of nested reaction fronts has been alluded to in other systems (Grube  $et\ al.$ , 1972; Russell and Parker, 1979; Singh  $et\ al.$ , 1982; Hawkins  $et\ al.$ , 1988; Hercod  $et\ al.$ , 1998; Drake  $et\ al.$ , 2009). In one extensively drilled granitic rock in Sweden for example (Drake  $et\ al.$ , 2009), pyrite was observed to oxidize in fractures to depths of 15 to 20 m because of deep circulation of  $O_2$ -charged meteoric fluids. Those authors noted that carbonate in fractures was also mostly leached from the upper 30 m, and they attributed this to circulation of  $CO_2$ -charged fluids.

Even deeper weathering has been reported where the water table is extremely deep and sulfide concentrations high. For example, zinc sulfide (ZnS) depletion has been reported to 60 m depth (Bowell *et al.*, 1996). Weathering profiles can even deepen to 1000 m (Ollier, 1984) when sulfides are concentrated and weathering advances for long durations because erosion is slow (Taylor and Eggleton, 2001). Furthermore, other more soluble sulfides (pentlandite, chalcopyrite, sphalerite, galena) can disappear deeper than pyrite (Butt and Zeegers, 1992). In fact, where water tables are falling, Ollier (1984) argues that weathering often proceeds to depths of hundreds of meters.

Sulfide weathering has also been reported to extend meters into the subsurface for sedimentary rocks near Shale Hills. For example, in Preston County, WV, weathering-induced depletion of pyrite-sulfur has been observed to depths of 6 m in sandstone, but locally in fractures to depths of 16 m (Grube *et al.*, 1972; Singh *et al.*, 1982). Depletion of calcite was also noted to depths similar to that of pyrite (compare Figure 11).

Like our model for Shale Hills, the depths of weathering of sulfides and carbonates have been attributed in some locations to reaction fronts that are subparallel to the land surface, roughly following the water table. For example, in pelitic mudstones in Japan, weathering of pyrite was deeper relative to the land surface under hilltops than hillslopes (Chigira, 1990). Those authors argued that weathering reactions largely depleted CO<sub>2</sub> by ~5m depth, O<sub>2</sub> by ~16 to 20 m depth, and H<sub>2</sub>SO<sub>4</sub> generated by pyrite oxidation by ~30–35 m depth. In general, the oxidation front and the water table were relatively close in depth. Separations between the two were attributed to the rapidity of climate-driven movements of the water table as compared to the slow rates of movement of reaction fronts (Chigira, 1990; Chigira and Sone, 1991; Chigira and Oyama, 1999; Oyama and Chigira, 1999).

In the work by Chigira and coworkers, depths of reaction fronts were affected by protolith permeability, the fluxes of the reactive gases CO<sub>2</sub> and O<sub>2</sub>, and the rates of infiltration of H<sub>2</sub>SO<sub>4</sub>. For example, the oxidation front in a more-permeable sandstone in Japan was observed at 32 to 37 m depth versus 16–20 m for a nearby less-permeable mudstone (Chigira and Sone, 1991). Likewise, an H<sub>2</sub>SO<sub>4</sub>-neutralization front (zeolite depletion) at 43 to 60 m depth in a permeable sandstone was deeper than the H<sub>2</sub>SO<sub>4</sub>-neutralization front (primary silicate depletion) observed in a nearby less-permeable mudstone (30–35 m depth). Grain size and permeability have similarly been hypothesized to control variable depths of oxidation from 8 to 20 m in other localities (Dixon *et al.*, 1982).

#### Fracture systems in the Appalachians

The nested reaction front hypothesis for Shale Hills is also bolstered by arguments in the literature concerning fracturing in valleys in the Appalachian region. In such valleys, groundwater flow may commonly be channelized by stress relief fractures because the intrinsic permeabilities of the cemented sandstones or shale rocks are very low (Wyrick and Borchers, 1981). Wyrick and Borchers (1981) report that in the Appalachian plateau, fluid penetrates largely along flat-lying stress relief fractures in the valley and vertical slump fractures along valley walls. Recharge to the aquifer occurs as surface runoff enters valley wall fractures. Although Shale Hills lies in the Valley and Ridge province rather than the plateau, similar fracturing features could be important.

Likewise, on the basis of their observations in the northeastern Appalachians, Ferguson and Hamel (1981) report that fracturing driven by valley formation dominates fluid flow patterns. Specifically, valley bottoms experience compression whereas valley walls experience extension (Ferguson and Hamel, 1981). As a result, the valley floor arches upward whereas the valley walls are deformed inward. As a consequence of these fractures, Ferguson and Hamel (1981) argue that along valley walls, sedimentary rocks are weathered to depths of 10 to 30 m, whereas under valley floors, the depth of weathering may be closer to 10–15 m. These patterns are somewhat similar to those described here for SSHO (Figure 11).

#### Is pyrite always the deepest reaction?

Several factors may explain why pyrite is often the deepest mineral reaction. First, O<sub>2</sub> diffuses quickly through the unsaturated zone (Feng *et al.*, 2002). Second, under the right conditions, pyrite oxidation is relatively fast (Nordstrom, 1982, 2000). Third, oxidation releases acid (see Reaction 3),

and the lower pH can hold more ferric iron in solution. In turn, dissolved ferric iron acts as an oxidant that accelerates the pyrite reaction, i.e. the reaction is autocatalytic. Finally, it is well known that sulfur-oxidizing bacteria can oxidize pyrite and accelerate the overall reaction. The acid generation, autocatalytic nature of iron(III), and the acceleration by bacteria mean that even small amounts of  $\rm O_2$  can initiate pyrite weathering at depth.

Furthermore, the pyrite reaction can then open porosity in an otherwise non-porous rock. Therefore, the rate of weathering advance into silicates or carbonates can be faster when pyrite is present compared to absent (Lichtner and Waber, 1992; Calmels *et al.*, 2007). In contrast, oxidation of ferrous silicates such as chlorite does not significantly open porosity or enhance dissolution of other minerals because such reactions do not release  $H_2SO_4$ .

However, sulfide oxidation is not always the deepest reaction. The relative positions of the reaction fronts for carbonate, pyrite, and silicates vary depending upon the rates of consumption of the reactants CO<sub>2</sub>, O<sub>2</sub>, and H<sub>2</sub>SO<sub>4</sub>. For example, in high-relief areas, Chigira and coworkers argued that oxygen and water flow in the same direction, causing the O<sub>2</sub>- and H<sub>2</sub>SO<sub>4</sub>-consumption fronts to move in the same direction but to become separated. They argued that sometimes the  $\mbox{H}_2\mbox{SO}_4$  reaction advances out ahead of pyrite oxidation. In contrast, in lowlands where O2 diffusion and water flow in opposite directions (downward and upward respectively), the fronts become almost coincident (Chigira and Sone, 1991; Chigira and Oyama, 1999). In contrast to these generalizations, we see at SSHO that the pyrite and carbonate fronts are separated at the valley but close under the ridge (Figure 11). Additional observational evidence is needed to understand these patterns but one likely explanation is that the coincidence or separation of the reaction fronts is a function not only of the direction of fluid flow but also the O<sub>2</sub> and CO<sub>2</sub> contents of the fluids in comparison to the R value of the rock (Equation 7).

# **Conclusions**

Chemical weathering represents the equilibration of rocks to Earth surface conditions, as catalyzed by biota. Throughout this paper we have ignored biological processes largely because we have no observations of the deep distribution of microbiota at SSHO. However, given that we know that both iron-reducing and -oxidizing bacteria are prevalent in many weathering systems including SSHO (Yesavage *et al.*, 2012), it is likely that many of the redox reactions in the subsurface we have discussed in this paper are also catalyzed by microorganisms. Regardless, the mineralogical, chemical, and isotopic variations described for the SSHO subsurface can be well explained by the hypothesis of nested chemical reaction fronts with or without biotic influences.

According to this hypothesis, acid and oxidant influxes beneath Shale Hills have created depletion zones of carbonate and pyrite respectively that form reaction fronts sub-parallel to the land surface. Such fronts are identified from depletion profiles that are either completely developed (mineral is 100% depleted at land surface, e.g. pyrite, carbonate) or incompletely developed (mineral still present at land surface, e.g. feldspar, illite, chlorite). Pyrite and carbonate depletion go to 100% completion because the mineral abundances are generally low and the reactions are fast relative to physical erosion of material; in contrast, clay mineral depletion is not complete at the land surface because clays are abundant and weathering rates are slow. The zones of depletion of pyrite and carbonate are deeper at the ridge than the valley: pyrite

concentrations return to parent values at depths of ~23 m (ridge) versus ~8–9 m (valley) and carbonate concentrations are insignificant to depths of ~22 m (ridge) versus ~2 m (valley). In contrast, the incompletely developed depletion profiles of the clays probably initiate at ~6–8 m depth under both ridge and valley and may be partly controlled by the occurrence of fracturing and fluid flow within a layer of that thickness.

Although oxidation of pyrite is almost complete many meters below the land surface at Shale Hills, the physical disaggregation of bedrock to form regolith occurs at much shallower depths. Therefore, disaggregation cannot be attributed to iron oxidation. Jin *et al.* (2011b) argued that significant weathering of illite initiates within 15 cm of the depth of disaggregation of saprock into regolith. (We define regolith to be material that can be hand-augered.) It is therefore possible that weathering of the Rose Hill shale initiates when the bedrock weathers to saprock at the depth where pyrite oxidation becomes significant, but that saprock transforms to regolith only where weathering of the dominant mineral – clay – becomes significant.

Given these arguments, we might refer to pyrite oxidation as the 'profile-initiating reaction' that starts the cascade of reactions producing soil, but that clay dissolution is the 'regolith-initiating reaction' that is the proximate cause of disaggregation and production of regolith. Of course, it bears repeating that our analysis here is made with little consideration of biotic influences. It is possible, for example, that the clay reactions are not driving regolith formation but rather that biotic processes (Roering *et al.*, 2002) such as tree root penetration followed by tree throw are the proximate drivers of disaggregation. In other words, tree root penetration might be the phenomenon that explains the depth of initiation of clay weathering rather than clay weathering driving the disaggregation.

If the hypothesis of nested reaction fronts is correct, then deep weathering at SSHO is controlled by biotic and abiotic influences on (i) the distribution of permeability; (ii) the rate of influx of meteoric water and the position of the water table; (iii) fluxes of O<sub>2</sub> and CO<sub>2</sub>; (iv) the initial distributions in concentrations of acid-producing (pyrite) and -neutralizing minerals (carbonate, clay). Pyrite oxidation at Shale Hills is the deepest reaction observed because O2 diffuses quickly through the unsaturated zone and because, once significant aqueous ferric iron is produced where water is present, oxidation is autocatalytic. Acceleration of the reaction in turn releases H2SO4 which causes increases in permeability, through-flux of CO<sub>2</sub>-charged fluids, and non-sulfide mineral dissolution. Based on our observations and the literature, we conclude that deep weathering in many localities is similar to SSHO in that it is driven by deep diffusion of O2 and the resulting oxidation reactions that open permeability to the flushing of meteoric fluids.

Acknowledgements—LJ and SLB acknowledge funding from NSF CHE-0431328 (PI: S. Brantley) for support for the Environmental Molecular Sciences Institute at Penn State (Center for Environmental Kinetics Analysis) and from NSF EAR-0725019 (PI: C. Duffy, Penn State) for the Susquehanna/Shale Hills Critical Zone Observatory. Logistical support was provided by the NSF-supported Susquehanna Shale Hills Critical Zone Observatory. This paper represents the senior thesis of MH who acknowledges support from the Department of Geosciences at Penn State. G. Holmes, E. Thomas, and J. Orlando contributed groundwater observations. The authors benefitted from discussions with T. White, C. Duffy, L. Ma (who provided the Zr data), N. West, A. Rose, and K. Singha. J. Gaillardet and an anonymous reviewer provided very helpful reviews. The Advanced Light Source is supported by the Director, Office of Science, DOE OBES under Contract No. DE-AC02-05CH11231.

# **Appendix**

**Table AI.** Comparison of Zr measured by ICP-AES and ICP-MS

Location, depth interval	Average depth (cm)	Zr (ppm) ICP- AES (PSU)	Zr (ppm) ICP- MS (SGS)
NPRT 00–10cm	5	240	235
NPRT 10-20 cm	15	225	216
NPRT 20-30 cm	25	250	246
NPRT 30-37 cm	33.5	250	263
NPRT 37-39 cm	38	205	194
NPVF 0-10 cm	5	265	259
NPVF 10-20 cm	15	235	265
NPVF 20-28 cm	24	230	236
NPVF 28-36 cm	32	215	205
NPVF 36-44 cm	40	225	224
NPVF 44-49 cm	46.5	215	210
NPVF 49-57 cm	53	220	222
NPVF 57-64 cm	60.5	210	211
NPVF 64-70 cm	67	215	216
NPVF 70-74 cm	72	220	230
NPVF 74-78 cm	76	205	228
NPVF 78-85 cm	81.5	210	215
NPVF 85-88 cm	86.5	215	209
NPVF 88-91 cm	89.5	225	226
NPVF 91-103 cm	97	210	207
NPVF 103-115 cm	109	220	239
NPVF 115-118 cm	116.5	225	236
NPMS3 0-8 cm	4	210	211
NPMS3 8–15 cm	11.5	225	230
NPMS3 15-26 cm	20.5	230	239
NPMS3 26-31 cm	28.5	225	241
NPMS3 31–35 cm	33	265	272
NPMS3 35-40 cm	37.5	200	208
SSOW 0-10 cm	5	140	141
SSOW 10-20 cm	15	140	141
SSOW 20-30 cm	25	155	148
SSOW 30-40 cm	35	165	167
SSOW 40-50 cm	45	190	187
SSOW 50-60 cm	55	200	221
SSOW 60-70 cm	65	200	202
SSOW 70-80 cm	75	195	173
SSOW 80–90 cm	85	170	160
SSOW 90–100 cm	95	160	153
SSOW 100-109 cm	104.5	205	191

All samples are samples of regolith that were hand augered. Depth intervals for samples are indicated in the sample names. Locations of samples (Figure 1) are indicated by the acronyms: NP, north planar transect; RT, ridge top; MS, mid slope; VF, valley floor; SSOW, stream sediment upper weir. ICP-MS measurements were completed at SGS Laboratory. Zr concentrations were measured by ICP-AES after samples were dissolved by lithium metaborate fusion in the Penn State Material Characterization Laboratory.

#### **REFERENCES**

- Abramoff MD, Magelhaes PJ, Ram SJ. 2004. Image processing with Image J. *Biophotonics International* **11**: 36–42.
- Anderson SP, Dietrich WE, Brimhall GH. 2002. Weathering profiles, mass balance analysis, and rates of solute loss: linkages between weathering and erosion in a small, steep catchment. *Geological Society of America Bulletin* **114**(9): 1143–1158.
- Anderson SA, Bales RC, Duffy CJ. 2008. Critical Zone Observatories: building a network to advance interdisciplinary study of Earth surface processes. *Mineralogical Magazine* 72: 7–10.
- Berner RA. 2006. GEOCARBSULF: a combined model for Phanerozoic atmospheric O<sub>2</sub> and CO<sub>2</sub>. *Geochimica et Cosmochimica Acta* **70**: 5653–5664.

- Bowell RJ, Areh EO, Laffoley NDA, Hanssen H, Abe S, Yao RK, Pohl D. 1996. Geochemical exploration for gold in tropical soils-four contrasting case studies from West Africa. Applied Earth Science 105: 12–33
- Brantley SL, Lebedeva M. 2011. Learning to read the chemistry of regolith to understand the Critical Zone. *Annual Review Earth Planetary Science* **39**: 387–416.
- Brantley SL, White AF. 2009. Approaches to modeling weathered regolith. In *Thermodynamics and Kinetics of Water–Rock Interaction*, Oelkers E, Schott J (eds). Reviews in Mineralogy and Geochemistry. Mineralogical Society of America and the Geochemical Society: Chantilly, VA.
- Brantley SL, Buss H, Lebedeva M, Fletcher RC, Ma L. 2011. Investigating the complex interface where bedrock transforms to regolith. *Applied Geochemistry* **26**: S12–S15. DOI. 10.1016/j.apgeochem.2011.03.017
- Brimhall G, Dietrich WE. 1987. Constitutive mass balance relations between chemical composition, volume, density, porosity, and strain in metasomatic hydrochemical systems: results on weathering and pedogenisis. *Geochimica et Cosmochimica Acta* **51**: 567–587.
- Butt CRM, Zeegers H. 1992. Regolith Exploration Geochemistry in Tropical and Subtropical Terrains, Handbook of Exploration Geochemistry. Elsevier Science: Amsterdam.
- Calmels D, Gaillardet J, France-Lanord C, Brenot A. 2007. Sustained sulfide oxidation by physical eorsion processes in the Mackenzie River basin: climatic perspectives. *Geology* 35: 1003–1006.
- Chigira M. 1990. A mechanism of chemical weathering of mudstone in a mountainous area. *Engineering Geology* **29**: 119–138.
- Chigira M, Oyama T. 1999. Mechanism and effect of chemical weathering of sedimentary rocks. *Engineering Geology* **55**: 3–14.
- Chigira M, Sone K. 1991. Chemical weathering mechanisms and their effects on engineering properties of soft sandstone and conglomerate cemented by zeolite in a mountainous area. *Engineering Geology* **30**: 195–219
- Dixon JB, Hossner, LR, Senkayi, AL, Egashira, K. 1982. Mineralogical properties of lignite overburden as they relate to mine spoil reclamation. In *Acid Sulfate Weathering*, Kittric JA, Fanning DS, Hossner LR (eds). Soil Science Society of America: Madison, WI.
- Drake H, Tullborg E, MacKenzie AB. 2009. Detecting the near-surface redox front in crystalline bedrock using fracture mineral distribution, geochemistry and U-series disequilibrium. *Applied Geochemistry* **24**: 1023–1039.
- Ebelmen JJ. 1845. Sur les produits de la décomposition des espèces minérales de la famille des silicates. *Annales des Mines* 7: 3–66.
- Eberl DD. 2009. User's guide to RockJock a program for determining quantitative mineralogy from powder X-ray diffraction data. In *Survey*, TUSG (ed). US Department of the Interior: Boulder, CO.
- Feldman C. 1983. Behavior of trace refractory minerals in the lithium metaborate fusion acid dissolution procedure. *Analytical Chemistry* 55: 2451–2453.
- Feng G, Wu L, Letey J. 2002. Evaluating aeration criteria by simultaneous measurement of oxygen diffusion rate and soil–water regime. *Soil Science* **167**: 495–503.
- Ferguson HF, Hamel JV. 1981. Valley stress relief in flat-lying sedimentary rocks. *Proceedings of the International Symposium on Weak Rock*, Tokyo; 1235–1240.
- Flueckinger LA. 1969. Report 176, Geology of a Portion of the Allensville Quadrangle, Centre and Huntingdon Counties, Pennsylvania. Bureau of Topographic and Geologic Survey, Commonwealth of Pennsylvania State Planning Board: Harrisburg, PA.
- Fold RL. 1960. Petrography and origin of Tuscarora Rose Hill, and Keefer formations, Lower and Middle Silurian of eastern west Virginia. *Journal of Sedimentary Petrology* **30**: 1–58.
- Gardner TW, Ritter JB, Shuman CA, Bell JC, Sasowsky KC, Pinter N. 1991. A periglacial stratified slope deposit in the valley and ridge province of central Pennsylvania, USA: sedimentology, stratigraphy, and geomorphic evolution. *Permafrost and Periglacial Processes* 2: 141–162.
- Goldich SS. 1984. Determination of ferrous iron in silicate rocks. *Chemical Geology* **42**: 343–347.
- Graham RC, Rossi AM, Hubbert KR. 2010. Rock to regolith conversion: producing hospitable substrates for terrestrial ecosystems. *GSA Today* **20**: 4–9.
- Grube J, Smith RM, Jencks EM, Singh RN. 1972. Significance of weathering in a Pennsylvanian sandstone to pollution from strip mines. *Nature* **236**: 70–71.

- Hawkins AB, Lawrence MS, Privett KD. 1988. Implications of weathering on the engineering properties of the Fuller's Earth formation. *Geotechnique* **38**: 517–532.
- Hercod DJ, Brady PV, Gregory RT. 1998. Catchment-scale coupling between pyrite oxidation and calcite weathering. *Chemical Geology* 151: 259–276.
- Jin L, Ravella R, Ketchum B, Bierman PR, Heaney P, White T, Brantley SL. 2010. Mineral weathering and elemental transport during hillslope evolution at the Susquehanna/Shale Hills Critical Zone Observatory. Geochimica et Cosmochimica Acta 74: 3669–3691.
- Jin L, Andrews DM, Holmes GH, Lin H, Brantley SL. 2011a. Opening the 'black box': water chemistry reveals hydrological controls on weathering in the Susquehanna Shale Hills Critical Zone Observatory. Vadose Zone Journal 10: 928–942. DOI. 10.2136/vzj2010.0133
- Jin L, Rother G, Cole DR, Mildner DFR, Duffy CJ, Brantley SL. 2011b. Characterization of deep weathering and nanoporosity development in shale – a neutron study. *American Mineralogist* 96: 498–512. DOI. 10.2138/am.2011.3598
- Jones JBJ, Isaac RA. 1972. Determination of sulfur in plant material using a Leco Sulfur Analyzer. *Journal of Agricultural and Food Chemistry* **20**(6): 1292–1294.
- Kak AC, Slaney M. 1988. Principles of Computerized Tomographic Imaging. IEEE Press: Piscataway, NJ.
- Kuntz B, Rubin S, Berkowitz B, Singha K. 2011. Quantifying solute transport behavior at the Shale Hills Critical Zone Observatory. Vadose Zone Journal 10: 1–15. DOI. 10.2136/vzj2010.0130
- Lebedeva MI, Fletcher RC, Brantley SL. 2010. A mathematical model for steady-state regolith production at constant erosion rate. *Earth Surface Processes and Landforms* **35**: 508–524.
- Liang Z, Ioannidis MA, Chatzis I. 2000. Geometric and topological analysis of three-dimensional porous media: pore space partitioning based on morphological skeletonization. *Journal of Colloid and Interface Science* **221**: 13–24.
- Lichter J. 1998. Rates of weathering and chemical depletion in soils across a chronosequence of Lake Michigan sand dunes. *Geoderma* **85**: 225–282.
- Lichtner PC, Waber N. 1992. Redox front geochemistry and weathering: theory with application to the Osamu Utsumi uranium mine, Pocos de Caldas, Brazil. *Journal of Geochemical Exploration* **45**: 521–564.
- Lin HS. 2006. Temporal stability of soil moisture spatial pattern and subsurface preferential flow pathways in the Shale Hills Catchment. *Vadose Zone Journal* **5**: 317–340.
- Lin HS, Zhou X. 2008. Evidence of subsurface preferential flow using soil hydrologic monitoring at the Shale Hills catchment. *European Journal of Soil Science* **59**: 34–49.
- Lin H, Kogelmann WJ, Walker C, Bruns MA. 2005. Soil moisture patterns in a forested catchment: a hydropedological perspective. *Geoderma* **131**: 345–368.
- Lynch JA. 1976. Effects of Antecedent Soil Moisture on Storm Hydrographs. Penn State University: University Park, PA.
- Ma L, Jin L, Brantley SL. 2011a. Geochemical behaviors of different element groups during shale weathering at the Susquehanna/Shale Hills Critical Zone Observatory. *Applied Geochemistry* **26**: S89–S93.
- Ma L, Jin L, Brantley SL. 2011b. How mineralogy and slope aspect affect REE release and fractionation during shale weathering in the Susquehanna/Shale Hills Critical Zone Observatory. *Chemical Geology* 290: 31–49.
- MacDonald NW, Burton AJ, Jurgensen MF, McLaughlin JW, Mroz GD. 1991. Variation in forest soil properties along a Great Lakes pollution gradient. *Soil Science Society of America Journal* **55**: 1709–1715.
- Masschaele B, Dierick M, Vlassenbroeck J. 2005. Octopus V8 Server-Client Tomography Reconstruction Software. Department of Subatomic and Radiation Physics, University of Gent: Gent.
- Matsuoka N, Murton JB. 2008. Frost weathering: recent advances and future directions. *Permafrost and Periglacial Processes* **19**: 195–210.

- Murton JB, Peterson R, Ozouf JC. 2006. Bedrock fracture by ice segregation in cold regions. *Science* **314**: 1127–1139.
- Nelson DW, Sommers LE. 1996. Total carbon, organic carbon, and organic matter. In *Methods of Soil Analysis, Part 3. Chemical Methods,* Spark DL (ed). Soil Science Society of America: Madison, WI.
- Nezat CA, Blum JD, Yanai RD, Hamburg SP. 2007. A sequential extraction to selectively dissolve apatite for determination of soil nutrient pools with an application to Hubbard Brook Experimental Forest, New Hampshire, USA. *Applied Geochemistry* **22**: 2406–2421.
- Nordstrom DK. 1982. Aqueous pyrite oxidation and the consequent formation of secondary iron minerals. In *Acid Sulfate Weathering*, Kral M (ed). Soil Science Society of America: Madison, WI.
- Nordstrom DK. 2000. Advances in the hydrogeochemistry and microbiology of acid mine waters. *International Geology Review* **42**: 499–515.
- Ollier C. 1984. Weathering. Longman: London.
- Oyama T, Chigira M. 1999. Weathering rate of mudstone and tuff on old unlined tunnel walls. *Engineering Geology* **55**: 15–27.
- Roering JJ, Almond P, Tonkin P, McKean J. 2002. Soil transport driven by biological processes over millennial time scales. *Geology* 30: 1115–1118.
- Rose AW, Cravotta CA. 1998. Coal mine drainage prediction and pollution prevention in Pennsylvania. Pennsylvania Department of Environmental Protection catalog #TN321.C6 1998. Pennsylvania Department of Environmental Protection: Harrisburg, PA. http://www.techtransfer.osmre.gov/NTTMainSite/Library/pub/cmdpppp.shtm
- Russell DJ, Parker A. 1979. Geotechnical, mineralogical and chemical interrelationships in weathering profiles of an overconsolidated clay. Quarterly Journal of Engineering Geology & Hydrogeology 12: 107–116.
- Singh RN, Grube J, Smith RM, Keefer RF. 1982. Relation of pyritic sandstone weathering to soil and minesoil properties. In *Acid Sulfate Weathering*, Kittrick JA (ed). Soil Science Society of America: Madison, WI.
- Szramek K, McIntosh JC, Williams EL, Kanduc T, Ogrinc N, Walter LM. 2007. Relative weathering intensities of calcite vs. dolomite in carbonate-bearing temperate zone watersheds: carbonate geochemistry and fluxes from catchments within the St. Lawrence and Danube River Basin. *Geochemistry, Geophysics, Geosystems* 8. DOI. 10.1029/2006GC00137
- Taylor G, Eggleton RA. 2001. *Regolith Geology and Geomorphology*. John Wiley & Sons: Chichester.
- Vandenbygaart AJ, Protz R. 1995. Soil genesis on a chronosequence, Pinery Provincial Park, Ontario. *Canadian Journal of Soil Science* **75**: 63–72.
- Vogel JC. 1993. Variability of carbon isotope fractionation during photosynthesis. In *Stable Isotopes and Plant Carbon–Water Relations*, Ehleringer JR, Hall AE, Farquhar GD (eds). Academic Press: San Diego, CA.
- White AF, Schulz MS, Lowenstern JB, Vivit DV, Bullen TD. 2005. The ubiquitous nature of accessory calcite in granitoid rocks: implications for weathering, solute evolution, and petrogenesis. *Geochimica et Cosmochimica Acta* **69**: 1455–1471.
- Williams EL, Szramek K, Jin L, Ku TCW, Walter LM. 2007. The carbonate system geochemistry of shallow groundwater/surface water systems in temperate glaciated watersheds (Michigan, USA): significance of open system dolomite weathering. *Geological Society of American Bulletin* 119: 515–528.
- Wyrick GG, Borchers JW. 1981. Hydrologic Effects of Stress-relief Fracturing in an Appalachian Valley, US Geological Survey Water-Supply Paper 2177. US Geological Survey: Reston, VA; 51.
- Yesavage TA, Fantle MS, Vervoort J, Mathur R, Jin L, Liermann LJ, Brantley SL. 2012. Fe cycling in the Shale Hills Critical Zone Observatory, Pennsylvania: an analysis of biogeochemical weathering and Fe isotope fractionation. *Geochimica et Cosmochimica Acta* **99**: 18–38. DOI. org/10.1016/j.gca.2012.09.029